Extensive longevity and DNA virus-driven adaptation in nearctic *Myotis* bats

Juan M Vazquez[1,2,20], M. Elise Lauterbur[3,4,20], Saba Mottaghinia[5], Léa Gaucherand[6], Sarah Maesen[5], Michael Singer[7], Sarah Villa[7], Melanie Bucci[3], Devaughn Fraser[8,9], Genavieve Gray-Sandoval[3], Zeinab R Haidar[10,111], Melissa Han[12], William Kohler[12], Tanya M. Lama[13], Amandine Le Corf[5], Clara Loyer[5], Dakota McMillan[1,14], Stacy Li[1,15], Johnathan Lo[15], Carine Rey[5], Samantha LR Capel[8], Kathleen Slocum[16], Melissa Sui[7], William Thomas[17], Janet Debelak Tyburec[18], Rachel Brem[19], Richard Miller[12], Michael Buchalski[8], Jose Pablo Vazquez-Medina[1], Sébastien Pfeffer[6], Lucie Etienne[6,21]*, David Enard[3,21,22]**, Peter H Sudmant[1,14,21,22,23]***

Affiliations:

1. Department of Integrative Biology, University of California, Berkeley, Berkeley, CA USA
2. Current affiliation: Department of Biology, Pennsylvania State University, State College, PA USA
3. Department of Ecology and Evolutionary Biology, University of Arizona, Tucson, AZ USA
4. Current affiliation: Department of Biology, University of Vermont, Burlington, VT USA
5. Centre International de Recherche en Infectiologie (CIRI), Inserm U1111, UCBL1, CNRS UMR5308, Ecole Normale Supérieure ENS de Lyon, Université de Lyon, Lyon, France
6. Université de Strasbourg, Architecture et Réactivité de l'ARN, Institut de Biologie Moléculaire et Cellulaire du CNRS, Strasbourg, France.
7. Department of Molecular and Cellular Biology, University of California, Berkeley, Berkeley, CA USA
8. Wildlife Genetics Research Unit, Wildlife Health Laboratory, California Department of Fish and Wildlife, Sacramento, CA, USA
9. Current affiliation: Wildlife Diversity Program, Wildlife Division, Connecticut Department of Energy and Environmental Protection, Burlington, CT, USA
10. Department of Biology, California State Polytechnic University, Humboldt, Arcata, CA USA
11. Current affiliation: Western EcoSystems Technology Inc, Cheyenne, WY USA
12. Department of Pathology and Clinical Laboratories, University of Michigan, Ann Arbor, MI USA
13. Department of Biological Sciences, Smith College, Northampton, MA USA
14. Department of Science and Biotechnology, Berkeley City College, Berkeley, CA USA
15. Center for Computational Biology, University of California, Berkeley, Berkeley, CA USA
16. Bat Conservation International, Austin, TX USA
17. Department of Ecology and Evolution, Stony Brook University, Stony Brook NY USA
18. Bat Survey Solutions, LLC, Tucson, AZ USA
19. Department of Plant and Microbial Biology, University of California, Berkeley, Berkeley, CA 94720, USA
20. These authors contributed equally
21. Senior author
22. These authors contributed equally
23. Lead contact

* Correspondence: lucie.etienne@ens-lyon.fr
** Correspondence: denard@arizona.edu
*** Correspondence: psudmant@berkeley.edu

Abstract

The genus *Myotis* is one of the largest clades of bats, and exhibits some of the most extreme variation in lifespans among mammals alongside unique adaptations to viral tolerance and immune defense. To study the evolution of longevity-associated traits and infectious disease, we generated cell lines and near-complete genome assemblies for 8 closely related species of *Myotis*. Using genome-wide screens of positive selection, analyses of structural variation, and functional experiments in primary cells, we identify new patterns of adaptation contributing to longevity, cancer resistance, and viral interactions in bats. We show that the recurrent evolution of longevity seen in *Myotis* leads to some of the highest predicted increases in cancer risk across mammals and demonstrate a unique DNA damage response in primary cells of the long-lived *M. lucifugus*. We also find evidence of abundant adaptation in response to DNA viruses - but not RNA viruses - in *Myotis* and other bats in sharp contrast with other mammals, potentially contributing to the role of bats as reservoirs of zoonoses. Together, our results demonstrate how genomics and primary cells derived from diverse taxa uncover the molecular bases of extreme adaptations in non-model organisms.

Keywords

Aging, Bats, Cancer, Evolutionary Biology, Functional Genomics, Immunity, Infectious Disease

Introduction

Bats (order *Chiroptera*) represent approximately 20% of all known mammalian species and are one of the most phenotypically diverse clades of mammals[1,2]. Since their emergence 60 million years ago[3–5], many bat lineages have independently evolved a wide variety of life history strategies and phenotypic traits, including exceptional changes in longevity, viral tolerance, and immune defense[6–11]. Such systems, in which shared traits have evolved *de novo* multiple times, are powerful resources for dissecting the genetic basis of phenotypes. Rigorous approaches to studying these traits, however, depend on high-quality, well-annotated genomes to test evolutionary and genomic hypotheses, and on experimental functional systems to validate these hypotheses.

The largest genus of bats - *Myotis* - is estimated to have emerged approximately 33 million years ago[12,13], and encompasses over 139 described species spanning six continents and a wide range of ecological niches[1,12–14]. *Myotis* species demonstrate some of the most extreme variation in lifespan amongst mammals[6,15–18], including a six-fold difference in lifespan between the longest-lived species (*M. brandtii*, 42 years[15,19], **Fig. 1A**) and the shortest-lived species (*M. nigricans*, 7 yrs[15,20]) which diverged approximately 10.6 million years ago[5,14,21,22]. In addition, *Myotis* species have been used as systems for investigating virus tolerance and other pathogen resistance[23–25] associated with the expansion and contraction of antiviral defenses[26–29], which have contributed to bats' ecological role as zoonotic reservoirs[10,11,30–33].

While studies on the genetic basis of longevity in short-lived model organisms have been crucial for identifying and dissecting several key aging pathways, comparative studies of exceptionally long-lived organisms have uncovered novel genes and pleiotropic effects governing lifespan[34–47]. Similarly, studies of infectious disease response are common and powerful in model organisms, but the lack of diversity and use of inbred lines limits their scope. Bats in particular present an important case study in, and opportunity to study, variation in virus adaptation strategies due to bats' role as zoonotic reservoirs and their specific resistance to viruses[43,48].

Here we combined comparative and functional approaches in *Myotis* to uncover genomic and functional evidence of adaptation to both aging-related and infectious diseases. Using near-complete genome assemblies, we identified significant structural variation encompassing stress response, immunity, and inflammation genes, including a trans-species copy number polymorphism of Protein kinase R (PKR). Additionally, we quantify relative intrinsic cancer risk across mammals and find that both ancestral taxa and extant species in *Myotis* are overrepresented at the extreme of increased relative cancer risk. Consistent with this observation, we identified pervasive selection of genes in longevity- and cancer-related processes throughout *Myotis*. We observed some of the strongest signatures of selection at immune-related genes, including strong evidence of adaptation in virus-interacting proteins in *Myotis* and other bats. In contrast to humans and other primates, in which virus adaptation is driven by interactions with RNA viruses[49], we find that virus adaptation in bats is driven by interactions with DNA viruses, implying that bats' exceptional immune adaptations are more protective against DNA viruses. This also highlights a fundamental discordance between the fitness impacts of viruses on humans vs bats. Together, our results suggest that pleiotropy and co-evolution of traits in *Myotis* has played a key role in the evolution of exceptional longevity and infectious disease resistance.

Results

High quality chromosome-level assemblies of 8 *Myotis* bat species

To study how lifespan and viral response have evolved in *Myotis*, we collected skin punches and derived primary cell lines from several North American ("Nearctic")[21] species (**Fig. 1A,C),** including from one of the longest-lived mammals, *Myotis lucifugus*[15]. Using these cell lines and flash frozen tissues we generated *de novo* haplotype-resolved, chromosome-scale genome assemblies for eight species (**Fig. 1A, Extended Data Fig. 1**) using a combination of long-read PacBio HiFi sequencing and HiC scaffolding. These genomes are highly contiguous, with an average of 98.6% of nucleotides assembled into 22-23 syntenic chromosome-scale scaffolds corresponding to the published karyotype[50] with an average QV of 66 (Extended Data Fig. 1; **Table S1**). These genomes have among the highest contig NG50 and lowest auNG scores of any *Chiroptera* genome published to date (**Fig. 1A, E**; **Extended Data Fig. 1**; **Table S1**). We identified an average of 27,536 protein coding genes per genome, with BUSCO[51,52] scores ranging from 98.2% to 98.5% (**Fig. 1D**). Using these annotations, we resolved the conflicting phylogenies of Nearctic *Myotis*[14,53–56] by using 1-to-1 orthologs of protein-coding genes across 534 mammalian genomes (**Table S2**) to build a time-calibrated, maximum likelihood tree of *Eutheria*. Our results conclusively resolve the relationship between known sister species (*M. lucifugus* and *M. occultus*; *M. yumanensis and M. velifer*; and *M. evotis* and *M. thysanodes*) with 100% bootstrap support at all nodes in the Nearctic *Myotis*. (**Fig. 1B**; **Extended Data Fig. 2A**; **Table S1**)

Across all 8 genomes, each autosome has been completely assembled telomere-to-telomere (T2T) in at least one species (**Fig. 1E**). Within assemblies, 29%-70% of chromosomes are fully assembled with an average of less than one gap per chromosome (**Table S1**). Overall, these fully annotated genomes represent some of the most contiguous mammalian assemblies to date.

Evolution of structural variation within constrained karyotypes

With our near-complete assemblies, we first sought to study the landscape of structural variation within the tightly-conserved karyotype seen in *Myotis*. With only six exceptions across over 60 studied species[57–61], all *Myotis* species have a conserved 2n=42 karyotype - a remarkable phenomenon for a genus spread across six

continents and 20 million years of divergence[1,2]. The conserved *Myotis* karyotype consists of three large autosomes and one small metacentric autosome; 17 small telocentric autosomes; and metacentric X and Y chromosomes[50,62]. Consistent with this broad cytological conservation, we find large scale synteny across the Nearctic *Myotis* in this study (**Fig. 2A**). However, structural variants (SVs) including inversions, duplications, and translocations are relatively common within chromosomes, especially adjacent to putative centromeric regions (**Fig. 2A, B**). This includes a ~20Mb block at the sub-telomeric end of Chr V15 that displays frequent and recurrent inversions and translocations across the Nearctic *Myotis*, and which contains a 10Mb locus that was recently identified as a potential target of recent selection by adaptive introgression[56] (**Extended Data Fig. 3D**).

Using SyRI[63], we identified between 6,813 - 8,013 SVs per Nearctic *Myotis* genome relative to their outgroup, *M. myotis*; 97 - 99% of these events were under 10Kb. In the three large autosomes, which constitute ~30% of the genome, we cataloged an average of 509 SVs (**Table S3**). In contrast, in the small autosomes, constituting ~65% of the genome, we observed an average of 316 events, highlighting the distinct structural evolution between these chromosome types with SVs found at 2-fold higher density in larger autosomes (**Table S3**). However, large (≥10Kb) duplications, large inverted duplications, and large inverted translocations were more common on small autosomes compared to the large autosomes (**Table S3**). We also quantified the distribution of transposable elements (TEs) across chromosomes (**Fig. 2B,C**). Consistent with prior observations in other Chiropteran genomes[64], LINE elements appeared to be enriched around the predicted centromere (**Fig. 2B**) with simulations showing that this trend is primarily limited to the long, metacentric autosomes (**Extended Data Fig. 3A**; **Table S3**). The concentration of segmental duplications was also significantly correlated with TE density in each species (linear regression, $p < 0.001$; **Fig. 2B,D; Extended Data Fig. 3B**) highlighting the importance of TEs in facilitating structural evolution. Together these results highlight high levels of structural variation coincident with mobile element activity occurring in the context of a highly constrained karyotype.

An actively segregating, trans-species copy number polymorphism of the antiviral factor Protein Kinase R, PKR

Among the duplicated loci identified in Nearctic *Myotis*, the gene Protein Kinase R (*PKR*/*EIF2AK2*) stood out as an interferon-stimulated gene with antiviral activity against both DNA and RNA viruses. While the functionality of this *Myotis*-specific duplication had been previously characterized[28], the absence of long-read sequencing data for *Myotis* has prevented a more detailed characterization of copy number and evolutionary history among Neartic *Myotis.* Using our near-complete genome assemblies, we fully resolved the sequence and structure of the two previously known haplotypes: H1, containing a single copy of *PKR* (*PKR2*); and H2, containing two tandemly duplicated copies of *PKR* (*PKR1* and *PKR2*; **Fig. 3A**). We also identified a third haplotype - H3 - with three tandem duplicates of *PKR* (*PKR1*, *PKR2*, and a third copy) present only in *M. californicus*. Remarkably, while 7 out of 9 *Myotis* species carried duplicated haplotypes, 5 of these cases were heterozygous for the duplicated haplotype (i.e. H1/H2 or H1/H3; **Fig. 3B**). Two *Myotis* individuals (*lucifugus* and *evotis*) only carried non-duplicated (i.e. H1/H1; **Fig. 3B**). To determine the evolutionary history of the duplicates, we used GeneRax[65] to construct a tree from alignments of all *PKR* gene copies across Neartic *Myotis*, using *Pipistrellus pygmaeus* as a non-*Myotis* outgroup (**Fig. 3C**). Our results suggest that *PKR2* is the ancestral copy of *PKR*, and that *PKR1* originated from a single duplication event at the root of *Myotis*. These results highlight that both the duplicated and unduplicated haplotypes have likely been segregating for tens of millions of years, representing an ancient trans-species polymorphism.

156 PKR is a stress response and innate immune factor that becomes active upon detection of dsRNA
157 through sensing, auto-phosphorylation and dimerization[66,67]. Active PKR shuts down protein translation and
158 restricts viral replication[66,67]. Although PKR1 and PKR2 are both expressed in basal or interferon-stimulated
159 *Myotis velifer* cells, only their independent functional impacts have previously been investigated[28]. Given the co-
160 expression and the complex haplotype diversity we identified in *Myotis*, we set out to determine whether the two
161 *PKR* copies act additively, synergistically, or as dominant negatives in several essential functions. We therefore
162 investigated the functional impact of the duplicates' co-expression on total PKR protein expression levels, cell
163 viability, inhibition of translation, antiviral restriction and homo/hetero-dimer formation (**Fig. 3D-H**). To pinpoint
164 the contribution of PKRs, we used a heterologous cell system[28] with PKR-KO Hela cells transfected with either
165 an empty pSG5 plasmid (control), or pSG5 encoding PKR1, PKR2, or PKR1+PKR2 from *Myotis myotis*
166 (myoMyo) or *Myotis velifer* (myoVel). In this system, PKR transfection leads to its autoactivation[28]. First, we
167 investigated PKR protein expression and found that, although *Myotis* Flag-PKR1 was expressed at lower levels
168 than Flag-PKR2, PKR1+PKR2 co-expression did not affect the overall PKRs' steady-state protein expression
169 levels (**Extended Data Fig. 4A**).

170 Second, we performed cell viability assays at two doses of transfected PKRs and found that cell viability
171 was only affected at high dose (**Extended Data Fig. 4D**). Third, using a luciferase reporter translational assay,
172 we found that PKR1+PKR2 coexpression led to an intermediate translation shutdown, showing neither
173 synergistic nor dominant negative effect of the PKR duplicates (**Fig. 3D**). Fourth, we tested PKR1+PKR2 co-
174 expression effects on infections by two different model RNA viruses: VSV-GFP (Vesicular stomatitis virus
175 encoding a GFP reporter[68], a representative of *Rhabdoviridae* family that is common in bats, including *Myotis*)
176 and SINV-GFP (Sindbis virus, a representative of *Togaviridae*) (**Fig. 3E-F**, **Extended Data Fig. 4C,E**). We found
177 that PKR1+PKR2 restricted viral infections to a similar, though slightly higher, extent as PKR1 or PKR2 alone
178 (**Fig. 3E-F; Extended Data Fig. 4C-D**, p>0.05). e recently duplicated PKR1s homodimerized, PKR1 and
179 PKR2 did not form heterodimers (**Fig. 3G-H** and **Extended Data Fig. 4B** in SINV condition). This suggests that,
180 since their duplication, divergence between *Myotis* PKR copies has been particularly strong at the protein-protein
181 interface hindering their capacity to form heterodimers.

182 Together, these results suggest that PKR1 and PKR2 are neither dominant negative nor synergistic with
183 each other, but rather act in a mostly additive form for their main cellular effector functions. Despite their capacity
184 to more broadly escape some DNA and RNA viral antagonists[28], increased cell toxicity at high PKR dose
185 suggests a possible tradeoff upon PKR duplication, which might participate in also explaining why PKR is rarely
186 duplicated in mammals. Consistent with this, PKR1 is known to be expressed at significantly lower levels in
187 *Myotis velifer* cells than PKR2 [28]. Altogether, these genomic and functional results unveil gene duplicates still
188 segregating across several *Myotis* species, possibly shaped by recent viral infections and cell toxicity tradeoff.

189 Genome-wide adaptation to DNA viruses

190 To further explore how viruses may have shaped the genomes of *Myotis* bats we tested for adaptive
191 signatures in virus-interacting proteins (VIPs) in *Myotis* and other bats. VIPs are host proteins that physically
192 interact with viral proteins (e.g. *CD45*, **Fig. 4A**), and can be proviral (contributing to viral infection, e.g. viral
193 receptors), antiviral (protective against viral infection, e.g. interferons), or both depending on infection stage and
194 virus type. VIPs commonly have major roles in basic host function, and as a result most host cell biological
195 pathways include VIPs. Previous studies investigating positive selection across mammals have found an
196 enrichment for adaptation among a set of 5,527 manually curated VIPs, defined as host proteins that have at
197 least one experimentally verified physical interaction with a viral protein, RNA, or DNA[69].

By calculating an enrichment score from the ratio of positive selection in VIPs compared to their matched control genes using BUSTED-MH[70], we found that, like other mammals, *Myotis* show an enrichment for adaptation at VIPs (**Fig. 4D; Table S5**). Physical host-virus interactions may not always result in fitness effects in the host. We therefore repeated our analysis using a gene set restricted to VIPs with experimental evidence of specific pro- or anti-viral effects, and thus with a stronger expectation of fitness effects. We observed an even stronger significant elevation in the ratio of positive selection in these proviral and antiviral VIPs (**Fig. 4B; Table S5**), but no elevation in this ratio in VIPs without experimental evidence of specific pro- or anti-viral effects (**Fig. 4C; Table S5**). This is consistent with the expectation of viral interaction as the cause of enrichment of positive selection in VIPs in bats[71]. We repeated this analysis using a dataset of 47 publicly-available non-*Myotis* bat genomes, and confirmed these same patterns across bats more broadly, even when excluding *Myotis* genomes (**Extended Data Fig. 5A**).

Previous work has suggested that bats may have different physiological responses to DNA and RNA viruses[72]. To determine if this was reflected in genomic VIP adaptation, we compared the enrichment of positive selection in VIPs that interact only with DNA viruses (DNA-only VIPs) to those that interact only with RNA viruses (RNA-only VIPs). Remarkably, we found that VIP adaptation in *Myotis* and other bats is driven by selection in DNA VIPs (**Fig. 4E, Extended Data Fig. 5B**) in marked contrast to the observed pattern in RNA VIPs, which show no evidence of genome-wide enrichment in adaptation (**Fig. 4F, Extended Data Fig. 5C**).

Adaptation to viral pathogens can also occur via gene copy number changes[73,74,75,76]. We tested whether VIPs were enriched among genes that were recently gained or lost throughout *Myotis* using the method of Huang *et al*. (2023) to test the cumulative per gene, per branch copy number changes and birth-death rates of VIPs compared to other non-VIP genes.[41] While the birth-death rate of VIP genes overall was no different than non-VIP genes ($p = 0.071$, **Extended Data Fig. 5D**), VIP genes were significantly more likely to have undergone expansions and/or contractions on at least one branch of the *Myotis* family ($p < 0.001$; **Fig. 4G**). Furthermore, we find that this pattern is driven exclusively by copy number changes in RNA-only VIPs, and not by changes in copy number of DNA-only VIPs (**Fig. 4H-I)**. This suggests that there is variation in gene family birth rates across species, but that VIPs are more dynamic across the Nearctic *Myotis* as a whole than other types of genes highlighting the importance of the viral immune response in recent *Myotis* evolution.

In contrast to what we observe in bats, VIP adaptation in humans is driven by positive selection in RNA - and not DNA - VIPs[69,77]. To investigate if DNA VIP-driven adaptation in bats is exceptional among mammals, we replicated these analyses across four other large mammalian orders that are well represented among publicly-available mammalian genomes: *Primates*, *Glires*, *Euungulata*, and *Carnivora*. We found that while other mammalian orders show a mix of adaptation enrichments in both RNA and DNA VIPs, none show an absence of genome-wide enrichment of adaptation in RNA VIPs as observed in bats (**Extended Data Fig. 5A-C**). These results highlight that bats, including *Myotis*, may have faced greater selective pressures from DNA viruses than from RNA viruses, in contrast to all other mammals.

Evolution of Lifespan & Peto's Paradox across Nearctic *Myotis*

Beyond their remarkable immune adaptations, bats are exceptional as the longest-lived clade of mammal after correcting for their body size[17,18,78], demonstrating a 1.5-fold range of lifespans within a 3-fold range of body sizes[6,78,79] ; *Myotis* species in particular exhibit the full dynamic range of bat lifespans within an even more narrow range of body sizes. While bats have been noted as an exception to the strong allometric scaling (positive

correlation with body size) of lifespan otherwise seen across mammals and other metazoans, this exception has not been tested using phylogenetically corrected statistics leveraging well-resolved phylogenies.

To test the hypothesis of non-allometric scaling of lifespan in bats, we modeled the evolution of body size and lifespan independently across a supertree of over 1000 placental mammals (*Eutheria*)[54] (**Fig. 5A-B; Extended Data Fig. 6A-B**; **Table S6**). We generally observed agreement between evolutionary patterns of body size and lifespan in the two simulations, such as in whales (*Cetacea*)[80,81], elephantids (*Proboscidea*)[37,82,83], and primates (**Fig. 5A-B**). However, while only minor changes were observed in their body size, we observed some of the largest and most-rapid changes in lifespan across mammals in bats (**Fig. 5A-B; Extended Data Fig. 6A-B**; **Table S6**). These changes are largely independent between species and genera, consistent with the theory of multiple independent increases in lifespan across bats. This is especially true in *Myotis*, where we saw many of the fastest increases in lifespan relative to their most recent ancestor, including for *Myotis grisescens* (4.15x increase, 100th percentile), *Myotis brandtii* (2.25x increase, 100th percentile), *Myotis lucifugus* (1.56x, 98th percentile), *Myotis myotis* (1.1x increase, 79nd percentile), and the *Myotis* common ancestor (1.26x increase, 92rd percentile) (**Fig. 5B, Extended Data Fig. 6B**).

We used phylogenetically-corrected generalized linear models and ANCOVA to quantify the relationship between body size and lifespan across mammals. We find that while non-bat mammals experience an average 0.159% increase in lifespan per 1% increase in body size, bats experience a 0.223% increase in lifespan years per 1% increase in body size, though these rates were not significantly different after phylogenetic correction (**Extended Data Fig. 6C-D**; pANCOVA: p=0.29). Together these results demonstrate that *Myotis* bats and their recent ancestors have evolved some of the most extreme increases in lifespan among mammals, despite similar allometric lifespan scaling of bats and mammals after phylogenetic correction.

Rapid changes in body size and lifespan can have major implications for the evolution of cancer risk and resistance across mammals. Within a species, lifetime *cancer risk* scales linearly with body size, and with lifespan by a power-law of exponent 6[84–87]. In contrast to a strong *within*-species correlation, when comparing *between*-species, there is only a weak correlation between body size and cancer risk - and no correlation between lifespan and cancer risk[87–91] - a phenomenon known as Peto's Paradox. This observation suggests that species with more cells or longer lifespans have adapted to reduce their cancer risks (i.e. increased cancer resistance) (**Fig. 5C**). We hypothesized that the very rapid evolution of increased lifespan in *Myotis* would thus result in a dramatic increase in their expected cancer risk compared to other mammals. Cancer risk can be explicitly measured as the prevalence of neoplasias in a species; however, there are very limited records for neoplasias in the literature, and none available for *Myotis* and other bats in family *Vespertilliodinae*[90,91].

An alternate approach is to quantify the Relative Intrinsic Cancer Risk (RICR) between extant mammals and their direct ancestors, calculated as the $\log_2$ ratio of cancer risk between the two nodes (**Fig. 5C,D**)[37,87]. In a scenario where a species has increased in either body size or lifespan relative to its direct ancestor, we would observe an increase in RICR corresponding to an increase in their potential cancer risk; this increase, in turn, is predicted to impart a proportional selective pressure on genes in cancer-related pathways to increase cancer resistance. We used our evolutionary estimates of body size and lifespan across *Eutheria* to quantify RICR across the placental mammals (**Fig. 5D**)[37], and found that bats were overrepresented in the top 10% of RICR (odds ratio 1.15), highlighting the impact of rapid lifespan evolution on cancer risk. This is consistent with recent pan-mammal and pan-vertebrate studies of cancer risk[90,91], which found that bats were present among the 20 species with the lowest rates of neoplasia, and not at all among the 20 species with the highest rates of neoplasia[91]. The longest-lived *Myotis* (*M. grisescens*: 39 yrs, 1st percentile; *M. brandtii*: 42 yrs, 2nd percentile; *M. lucifugus*: 36 yrs, 4th pct) and their most recent common ancestors (*lucifugus-occultus*: ~26 yrs, 8th pct;

Myotis common ancestor: ~22 yrs, 14th pct) demonstrated some of the most pronounced increases in RICR among mammals (**Fig. 5D; Table S6**). Similar to other extreme cases of body size and lifespan in vertebrates[37,39,44,46,92–96], the pronounced changes in RICR seen in *Myotis* imply strong selective pressure to evolve cancer resistance mechanisms at multiple points across *Chiroptera* in general, and within *Myotis* in particular.

Evolutionary signatures of cancer resistance and pleiotropy with DNA virus adaptations in *Myotis*

We hypothesized that the extreme changes in RICR observed throughout the *Myotis* phylogeny should exert a selective pressure on genes associated with cancer processes. Using aBSREL[97] to test for selection at terminal and internal branches within *Myotis*, we found that at FDR<=5%, an average of 5.46% of protein-coding genes had at least one region under positive selection per node (omega >1); in contrast, an average of 20.8% of protein-coding genes per node had all regions with an omega less than 1, suggesting negative selection (**Table S7**). Genes under selection were enriched for several pathways involved in immunity, cancer, and aging (**Table S7**), with many sitting at the intersection of multiple processes, including members of the Cluster of Differentiation (CD) family, Serpin family, insulin signaling pathway, redox repair, and iron storage (**Extended Data Fig. 6E; Table S7**), suggesting possible pleiotropic influences on genes under selection.

We quantified the contribution of genes under selection to pathways associated with the hallmark of cancer[98–100] by measuring the proportion of cancer-associated pathways overrepresented among genes under selection throughout the phylogeny (**Fig. 5E**). Consistent with the observation that most nodes within *Myotis* demonstrate increases in RICR, we observed that most nodes within nearctic *Myotis* were enriched for cancer hallmark pathways among genes under selection, especially at the recent ancestors of the longest-lived species (e.g. *M. lucifugus, M. occultus*; **Fig. 5E**). Furthermore, when considering the union of all genes under selection in the evolutionary history of each species since their common ancestor, we observed significant enrichments in the representation of cancer-associated pathways in many of the lineages with the greatest increases in RICR (*M. lucifugus*, *M. occultus, M. evotis, M. yumanensis;* **Fig. 5F, Extended Data Fig. 6F**). This suggests that selection in genes involved in cancer-related processes occurred concurrently with the recurrent increases in lifespan and RICR seen in this clade.

The longest-lived bat in our study, *M. lucifugus*, had an overrepresentation of pathways specifically associated with DNA double-strand break (DSB) repair when looking at both lineage-wide and node-specific enrichments in positive selection using the Reactome database[101] (**Fig. 5G; Table S7**). This includes 35 out of 65 genes in the high-fidelity Homologous Recombination Repair pathway, and 21/37 members of the Homology-Directed Repair via Single Strand Annealing (**Fig. 5G; Extended Data Fig. 6E; Table S7**). These results suggest that *M. lucifugus* might have an enhanced response to DNA DSBs relative to other bats. To test this hypothesis, we assessed the tolerance of *M. lucifugus* to neocarzinostatin, a potent radiomimetic agent that induces DNA double-strand breaks (**Fig. 5H**), compared to *M. evotis*, three non-*Myotis* bats (*Eidolon helvum, Pteropus rodrigensis,* and *Rousettus lanosus*). At low doses of neocarzinostatin, *M. lucifugus* was the only species tested showing sensitivity to neocarzinostatin after 24 hours, with a drop in viability and concomitant increase in apoptosis. At high doses, *M. lucifugus* had the highest level of apoptosis and the greatest drop in viability of all the bats tested. This is consistent with other long-lived species, including elephants[35,36,102], naked mole rats[45], and bowhead whales[39,103], where longevity and RICR are associated with an increased ability to clear out damaged cells.

To better understand the genes that may be driving this difference, we examined RNA expression in *M. lucifugus* cells after 6 and 18 hours of treatment with 100uM NCS. As expected, at 6 hours we observe up-regulation of genes associated with cell cycle arrest (e.g. *MDM2*, *CDKN1A*) and cell death (e.g. *BAX*),and down-regulation of genes in pathways associated with cell division and growth at 6 hours. At 18 hours, we observe up-regulation of genes in pathways associated with cellular stress response and continued down-regulation of the cell cycle (**Fig. 6A-D, Extended Data Fig. 7A, Table S9**). At 6 hours, however, we also observed down-regulation of genes associated with DNA damage repair and synthesis, which together with the up-regulation of *BAX* is consistent with the observed sensitivity to NCS in *M. lucifugus*.

Unexpectedly, however, we observed that the strongest pathway enrichment in our DNA-damage RNA-seq data were genes associated with the innate immune response, including genes in the PI3K/AKT pathway (**Fig. 6C-D, Table S9**). We hypothesized that the observed relationship between the unique DNA damage response of *M. lucifugus* may be due to pleiotropy with DNA VIPs and selection in these genes. Indeed, we observed that there was a highly significant enrichment for genes that are differentially expressed after NCS treatment and DNA-only VIPs (p=3.34e-5, **Fig. 6E**; α=0.0245, **Extended Data Fig. 7B**). The genes at the intersection of DNA-only VIPs and NCS response are overrepresented in pathways associated with the cell cycle, senescence, transcription, and DNA damage repair (**Fig. 6F**). To test how selection may have impacted these pleiotropic signatures, we repeated these analyses only considering genes under selection in *Myotis lucifugus*. The intersection between DNA-only VIPs and NCS-DE genes remained highly significant (p=1.88e-3, **Extended Data Fig. 7C**) with only three pathways remaining enriched at FDR<=0.05: Cell Cycle, DNA Damage Repair, and Deubiquination (**Fig. 6G**); DNA-only VIP genes which are not NCS-responsive did not show these signatures (**Extended Data Fig. 7D-G).** Together these results suggest that selection on the innate immune response may drive *agonistic* pleiotropy in aging-associated traits like DNA damage response and cell cycle regulation.

Discussion

Bats are widely known for their long lifespan, cancer resistance, and viral tolerance[6,10,11,43,78,90,104–106]. As highly complex and pleiotropic processes, the genes and mechanisms underlying these phenotypes can be challenging to identify, especially for rapidly-evolving phenotypes such as host-pathogen interactions. Here we outline an approach that enables functional comparative biology by generating cell lines from wing punches of wild caught bats for genome assembly, comparative genomics, and functional follow up. Cell lines are generated from minimally-invasive biopsies collected in the field thus avoiding disturbing natural populations. Using this approach, we identify new patterns of adaptation contributing to longevity, cancer resistance, and viral interactions in bats, and demonstrate a unique DNA damage response in primary cells of the long-lived *M. lucifugus.* Given the high density of bat species concentrated at single locations world-wide[107,108] it is feasible to collect wing punches from a large number of individuals across a wide phylogenetic range; these wing punches can be used to generate cell lines and sequencing libraries for reference genomes in a matter of weeks. This approach is useful to expand genetic resources across the tree of life[109–111] and for conservation genomics. As this approach can generate genomic resources from minimal material gathered via non-lethal sampling, it is also well-suited for the study of rare or endangered species for which acquiring sufficient amounts of material can be challenging.

The evolution of body size and lifespan across mammals - and the rapid evolution of lifespan in *Yinpterochiroptera* in particular - has major implications for the co-evolution of cancer risk and resistance. While

363 models of body size evolution are well-studied in mammals[7,37,82,112] the evolution of lifespan is less well
364 understood. We find that *Myotis* demonstrates an increased rate of change in lifespan given body size compared
365 to other mammals. This altered scaling of longevity in *Myotis* has dramatic consequences for their intrinsic, per-
366 cell cancer risk and for the evolution of tumor-suppressor genes and pathways. While cancer risk scales linearly
367 with body size, it scales with age as a power law of 6[84,87,88]. Meanwhile, while mammalian body sizes span a 10^6
368 range of masses, they only span a 10^2 range of lifespans[16,113]. Unlike other systems where the evolution of
369 cancer resistance has been driven by rapid changes in body size[35–37,44,92,96], the body size of *Myotis* has not
370 significantly changed since their common ancestor. Instead, the rapid and repeated changes in lifespan across
371 an order of magnitude in *Myotis* lead to some of the most significant changes in intrinsic cancer risk seen across
372 mammals.

373 Bats are also important models for understanding infectious disease response and immune adaptation
374 because of their unique resistance to viruses and role as zoonotic reservoirs[31,72,114]. Here, we show that while
375 bats have adapted to both DNA and RNA viruses, they demonstrate a remarkable dominance in adaptations to
376 DNA viruses. This is in contrast to humans and other primates, in which adaptation to RNA viruses
377 dominates[49,77]. While bats are known to mount adaptive immune responses to some RNA viruses, this suggests
378 that adaptations in bats' innate and adaptive immune systems, such expansions in *MHC-I* and *APOBEC3*, or the
379 loss of the *PYHIN* gene family[48], may be sufficient as a first line of defense to protect against the fitness impacts
380 of some RNA viruses, but not against DNA viruses. This is consistent with previous observations that most
381 zoonoses, including those hosted by bats, are RNA viruses[10] and that bats are more likely than other mammals
382 to asymptomatically harbor RNA viruses, while being more susceptible themselves to other pathogens such as
383 fungi[72]. We also recapitulate and expand on previous results related to positive selection in immune genes and
384 immune gene family expansion, contraction, and loss. In addition, we demonstrate complex patterns of structural
385 variation in immune genes, including a segregating duplication of the Protein Kinase R gene (*PKR*), a major
386 protein involved in the antiviral innate immune system, that has functional relevance in its activity against both
387 DNA and RNA viruses[28]. By resolving individual haplotypes in nine *Myotis* species, we were able to confirm a
388 single duplication event at the origin of *Myotis PKR1* and *PKR2*. We further demonstrate the functional
389 implications of copy number variation in *PKR*, including differences in copy expression and an additive effect on
390 cellular effector functions.

391 Multiple hypotheses have been proposed to connect the unique physiology and ecology of bats with the
392 evolution of remarkable adaptations such as viral infection tolerance, stress tolerance, and exceptional
393 longevity[104]. Hypothesized drivers of disease resistance and longevity evolution in bats include the evolution of
394 flight (e.g. "flight as fever" hypothesis[115], though this hypothesis has recently been critiqued[116]), the disposable
395 soma hypothesis[117]; metabolic state[118]; torpor[6]; and other adaptations to specific environments[9,119–121].
396 Additionally, many studies have highlighted the intersection of these traits, including a relationship between
397 hibernation and both longevity[6,114] and infectious disease resistance[72,114]. Our results are consistent with an
398 *agonistic* pleiotropy hypothesis, wherein genetic adaptations for many specific traits (e.g. DNA virus innate
399 immunity) may prove beneficial to other seemingly-unrelated traits (e.g. cancer resistance, cellular homeostasis,
400 longevity). Importantly, bats are also the only mammal to harbor active DNA transposons, the suppression of
401 which may also contribute to signatures of selection in DNA-interacting VIPs.

402 Consistent with the agonistic pleiotropy hypothesis, many of the genes and pathways highlighted in this
403 study have been found to play vital roles across physiological traits in bats and other species. For example, two
404 genes under selection in nearctic *Myotis* - *FTH1* and *IGFN1* - have been implicated in functional studies as key
405 hibernation genes[122–124], viral interacting proteins[125–128], and as pro-longevity genes[129–131]. Similarly, many DNA
406 VIPs such as *BRCA1/2* and *POLG* are core DNA maintenance genes essential for cancer resistance and

longevity[45,132–138]. Such essential genes are generally under increased constraint; however, it is possible that external pressures such as viral infection and active DNA transposable elements, are shaping the fitness landscape of these essential genes such that novel optimizations become accessible to evolutionary processes[139]. Beyond individual genes, many of the overarching pathways under selection in *Myotis*, such as those associated with inflammation, senescence, and ferroptosis lie directly at the intersection of aging-related immune processes[43,48,124,129,140–147]. While together our results suggest the possibility that traits such as cancer risk, cellular homeostasis, and antiviral response have evolved in tandem due to pleiotropic selection at overlapping points in bats' evolutionary histories, further functional validation will be required to disentangle the functional impacts of these genetic changes and disambiguate the drivers of selection.

Acknowledgements

PacBio HiFi sequencing was done by the DNA Technologies and Expression Analysis Cores at the UC Davis Genome Center (NIH SIG 1S10OD010786-01). Analyses were performed using the High Performance Computing (HPC) resources at the University of Arizona (supported by the University of Arizona TRIF, UITS, and Research, Innovation, and Impact (RII); maintained by the UArizona Research Technologies department); the Savio computational cluster resource provided by the Berkeley Research Computing program at the University of California, Berkeley (supported by the UC Berkeley Chancellor, Vice Chancellor for Research, and Chief Information Officer); and the Vermont Advanced Computing Core at . We thank the members of the LP2L team (CIRI) for helpful discussions.

MEL was funded by NSF PRFB #2010884, and a Dovetail Tree of Life Grant. JMV was funded by NSF PRFB #2109915, NIH NIA T32AG000266, and NIA 1K99AG088361. DE was funded by NIH NIGMS MIRA grant 5R35GM142677. PHS was funded by NIH NIGMS R35GM142916 and by the Vallee Scholars Award. LE was funded by a grant from the Agence Nationale de la Recherche (ANR, #ANR-202-CE15-0020-01 to LE) and CNRS MITI These Internationale (to M.S. and L.E.). SP is funded by the ANR (ANR-21-CE35-0018-01) and by the Interdisciplinary Thematic Institute IMCbio+ supported by IdEx Unistra (ANR-10-IDEX-0002), by SFRI-STRAT'US project (ANR-20-SFRI-0012) and EUR IMCBio (IMCBio ANR-17-EURE-0023) under the framework of the French Investments for the Future Program. LE and DE were further funded by a grant from the Joint Call for Proposals between the CNRS and the University of Arizona (International Research Center, IRC, 2021-2024). LE, DE, PHS and SP were further funded by the International Research Project (IRP) RAPIDvBAT from the CNRS, the University of Arizona and the University of California, Berkeley. LG was funded by a postdoctoral fellowship from the Fondation pour la Recherche Médicale (FRM, #SPF202209015746).

Image attributions for the bat photos featured in Fig. 1: J. Scott Altenbach (*M. thysanodes*); M. Elise Lauterbur (*M. occultus, M. velifer*); U.S. National Park Service (*M. auriculus*); Frank Carey (*M. californicus*); Michael Durham (*M. evotis*); J. N. Stuart (*M. volans*); and SMBishop & the Wikimedia Foundation (*M. lucifugus*).

Author Contributions:

Conceptualization, J.M.V., M.E.L., D.E., P.H.S., L.E., D.F., M.B.; Methodology, J.M.V., M.E.L., D.E., P.H.S., L.E., G.G.S.; Software, J.M.V., M.E.L., D.E., P.H.S., L.E., T.M.L.; Validation, J.M.V., M.E.L., D.E., P.H.S., L.E., J.P.V.M.; Formal Analysis, J.M.V., M.E.L., D.E., P.H.S., L.E., S.M., A.L.C., D.M., S.V.; Investigation, J.M.V., M.E.L., S.M., M.B., D.F., G.G.S., L.G., Z.R.H., M.H., W.K., T.M.L., A.L.C., C.L. S.M., D.M., S.L., J.L., C.R., S.L.R.C., M.S., K.S., W.T., J.D.T., S.V., R.M., M.B., J.P.V.M., S.P.,

L.E., D.E., P.H.S.; Resources, J.M.V., M.E.L., D.E., P.H.S., L.E., M.B., D.F., G.G.S., L.G., Z.R.H., M.H., W.K., T.M.L., A.L.C., S.M., D.M., S.L., J.L., C.R., S.L.R.C., M.S., K.S., W.T., J.D.T., S.V., R.M., M.B.; Data Curation, J.M.V., M.E.L., S.M., M.B., D.F., G.G.S., L.G., Z.R.H., M.H., W.K., T.M.L., A.L.C., S.M., D.M., S.L., J.L., C.R., S.L.R.C., M.S., K.S., W.T., J.D.T., S.V., R.M., M.B., J.P.V.M., S.P., L.E., D.E., P.H.S.; Writing - Original Draft, J.M.V., M.E.L., D.E., P.H.S., L.E., S.M., J.L.; Writing - Review & Editing, J.M.V., M.E.L., S.M., M.B., D.F., G.G.S., L.G., Z.R.H., M.H., W.K., T.M.L., A.L.C., S.M., D.M., S.L., J.L., C.R., S.L.R.C., M.S., K.S., W.T., J.D.T., S.V., R.M., M.B., J.P.V.M., S.P., L.E., D.E., P.H.S.; Visualization, J.M.V., M.E.L., D.E., P.H.S., L.E., S.M., A.L.C.; Supervision, J.M.V., M.E.L., D.E., P.H.S., L.E.; Project Administration, J.M.V., M.E.L., D.E., P.H.S., L.E.; Funding Acquisition, J.M.V., M.E.L., D.E., P.H.S., L.E.

Declaration of Interests:

The authors declare no competing interests.

References

1. Wilson, D. E. & Reeder, D. M. *Mammal Species of the World: A Taxonomic and Geographic Reference*. (JHU Press, 2005).
2. Simmons, N. B. & Cirranello, A. L. Bat Species of the World: A Taxonomic and Geographic Database. https://batnames.org/.
3. Teeling, E. C., Hedges, S. B. & Kumar, S. Bats (Chiroptera). *The timetree of life* 499–503 (2009).
4. Rietbergen, T. B. *et al.* The Oldest Known Bat Skeletons and Their Implications for Eocene Chiropteran Diversification. *PLoS One* **18**, e0283505 (2023).
5. Kumar, S., Stecher, G., Suleski, M. & Hedges, S. B. TimeTree: A Resource for Timelines, Timetrees, and Divergence Times. *Mol. Biol. Evol.* **34**, 1812–1819 (2017).
6. Wilkinson, G. S. & Adams, D. M. Recurrent Evolution of Extreme Longevity in Bats. *Biol. Lett.* **15**, 20180860 (2019).
7. Moyers Arévalo, R. L., Amador, L. I., Almeida, F. C. & Giannini, N. P. Evolution of Body Mass in Bats: Insights from a Large Supermatrix Phylogeny. *J. Mamm. Evol.* **27**, 123–138 (2020).
8. Datzmann, T., von Helversen, O. & Mayer, F. Evolution of Nectarivory in Phyllostomid Bats (Phyllostomidae Gray, 1825, Chiroptera: Mammalia). *BMC Evol. Biol.* **10**, 165 (2010).
9. Camacho, J. *et al.* Sugar assimilation underlying dietary evolution of Neotropical bats. *bioRxiv*

475 2023.07.02.547432 (2023) doi:10.1101/2023.07.02.547432.
476 10. Hayman, D. T. S. *et al.* Ecology of zoonotic infectious diseases in bats: current knowledge and
477 future directions. *Zoonoses Public Health* **60**, 2–21 (2013).
478 11. Irving, A. T., Ahn, M., Goh, G., Anderson, D. E. & Wang, L.-F. Lessons from the host defences of
479 bats, a unique viral reservoir. *Nature* **589**, 363–370 (2021).
480 12. Morales, A. E., Ruedi, M., Field, K. & Carstens, B. C. Diversification rates have no effect on the
481 convergent evolution of foraging strategies in the most speciose genus of bats, Myotis. *Evolution*
482 **73**, 2263–2280 (2019).
483 13. Gunnell, G. F., Smith, R. & Smith, T. 33 Million Year Old Myotis (Chiroptera, Vespertilionidae) and
484 the Rapid Global Radiation of Modern Bats. *PLoS One* **12**, e0172621 (2017).
485 14. Ruedi, M. *et al.* Molecular Phylogenetic Reconstructions Identify East Asia as the Cradle for the
486 Evolution of the Cosmopolitan Genus Myotis (Mammalia, Chiroptera). *Mol. Phylogenet. Evol.* **69**,
487 437–449 (2013).
488 15. Tacutu, R. *et al.* Human Ageing Genomic Resources: Integrated Databases and Tools for the
489 Biology and Genetics of Ageing. *Nucleic Acids Res.* **41**, D1027–D1033 (2013).
490 16. Jones, K. E. *et al.* PanTHERIA: A Species-Level Database of Life History, Ecology, and
491 Geography of Extant and Recently Extinct Mammals. *Ecology* **90**, 2648–2648 (2009).
492 17. Austad, S. N. Methusaleh's Zoo: How Nature Provides Us with Clues for Extending Human Health
493 Span. *J. Comp. Pathol.* **142**, S10–S21 (2010).
494 18. Austad, S. N. & Fischer, K. E. Mammalian Aging, Metabolism, and Ecology: Evidence from the
495 Bats and Marsupials. *J. Gerontol.* **46**, B47–53 (1991).
496 19. Podlutsky, A. J., Khritankov, A. M., Ovodov, N. D. & Austad, S. N. A new field record for bat
497 longevity. *J. Gerontol. A Biol. Sci. Med. Sci.* **60**, 1366–1368 (2005).
498 20. Wilson, D. E. & Tyson, E. L. Longevity Records for Artibeus Jamaicensis and Myotis Nigricans. *J.*
499 *Mammal.* **51**, 203 (1970).
500 21. Stadelmann, B., Lin, L.-K., Kunz, T. H. & Ruedi, M. Molecular Phylogeny of New World

\emphMyotis (Chiroptera, Vespertilionidae) Inferred from Mitochondrial and Nuclear DNA Genes. *Mol. Phylogenet. Evol.* **43**, 32–48 (2007).

22. Agnarsson, I., Zambrana-Torrelio, C. M., Flores-Saldana, N. P. & May-Collado, L. J. A Time-Calibrated Species-Level Phylogeny of Bats (Chiroptera, Mammalia). *PLoS Curr.* **3**, RRN1212 (2011).
23. Armero, A. *et al.* Myotis Fimbriatus Virome, a Window to Virus Diversity and Evolution in the Genus Myotis. *Viruses* **14**, 1899 (2022).
24. He, X. *et al.* Establishment of Myotis Myotis Cell Lines - Model for Investigation of Host-Pathogen Interaction in a Natural Host for Emerging Viruses. *PLoS One* **9**, e109795 (2014).
25. Seltmann, A. *et al.* Differences in Acute Phase Response to Bacterial, Fungal and Viral Antigens in Greater Mouse-Eared Bats (Myotis Myotis). *Sci. Rep.* **12**, 15259 (2022).
26. Hayward, J. A. *et al.* Unique Evolution of Antiviral Tetherin in Bats. *J. Virol.* **96**, e0115222 (2022).
27. Fernandes, A. P., Águeda-Pinto, A., Pinheiro, A., Rebelo, H. & Esteves, P. J. Evolution of TRIM5 and TRIM22 in Bats Reveals a Complex Duplication Process. *Viruses* **14**, (2022).
28. Jacquet, S. *et al.* Adaptive duplication and genetic diversification of protein kinase R contribute to the specificity of bat-virus interactions. *Sci Adv* **8**, eadd7540 (2022).
29. Jacquet, S., Pontier, D. & Etienne, L. Rapid Evolution of HERC6 and Duplication of a Chimeric HERC5/6 Gene in Rodents and Bats Suggest an Overlooked Role of HERCs in Mammalian Immunity. *Front. Immunol.* **11**, 605270 (2020).
30. Chomel, B., Stuckey, M., Boulouis, H. & Aguilar Setién, Á. Bat-Related Zoonoses. *Zoonoses - Infections Affecting Humans and Animals* 697–714 (2014) doi:10.1007/978-94-017-9457-2_28.
31. Guth, S. *et al.* Bats host the most virulent-but not the most dangerous-zoonotic viruses. *Proc. Natl. Acad. Sci. U. S. A.* **119**, e2113628119 (2022).
32. Williams, E. P. *et al.* Common themes in zoonotic spillover and disease emergence: Lessons learned from bat- and rodent-borne RNA viruses. *Viruses* **13**, 1509 (2021).
33. Mollentze, N. & Streicker, D. G. Viral zoonotic risk is homogenous among taxonomic orders of

527 mammalian and avian reservoir hosts. *Proc. Natl. Acad. Sci. U. S. A.* **117**, 9423–9430 (2020).
528 34. Kolora, S. R. R. *et al.* Origins and Evolution of Extreme Life Span in Pacific Ocean Rockfishes.
529 *Science* **374**, 842–847 (2021).
530 35. Sulak, M. *et al.* Correction: TP53 copy number expansion is associated with the evolution of
531 increased body size and an enhanced DNA damage response in elephants. *Elife* **5**, (2016).
532 36. Vazquez, J. M., Sulak, M., Chigurupati, S. & Lynch, V. J. A Zombie LIF Gene in Elephants Is
533 Upregulated by TP53 to Induce Apoptosis in Response to DNA Damage. *Cell Rep.* **24**, 1765–1776
534 (2018).
535 37. Vazquez, J. M. & Lynch, V. J. Pervasive duplication of tumor suppressors in Afrotherians during
536 the evolution of large bodies and reduced cancer risk. *Elife* **10**, e65041 (2021).
537 38. Davies, K. T. J. *et al.* Molecular Evolution of Growth Hormone and Insulin-like Growth Factor 1
538 Receptors in Long-Lived, Small-Bodied Mammals. *Gene* **549**, 228–236 (2014).
539 39. Vazquez, J. M., Kraft, M. & Lynch, V. J. A CDKN2C retroduplication in Bowhead whales is
540 associated with the evolution of extremely long lifespans and alerted cell cycle dynamics. *bioRxiv*
541 2022.09.07.506958 (2022) doi:10.1101/2022.09.07.506958.
542 40. Foote, A. D. *et al.* Convergent evolution of the genomes of marine mammals. *Nat. Genet.* **47**, 272–
543 275 (2015).
544 41. Huang, Z. *et al.* Duplications of Human Longevity-Associated Genes Across Placental Mammals.
545 *Genome Biol. Evol.* **15**, (2023).
546 42. Li, S., Vazquez, J. M. & Sudmant, P. H. The evolution of aging and lifespan. *Trends Genet.* **39**,
547 830–843 (2023).
548 43. Jebb, D. *et al.* Six reference-quality genomes reveal evolution of bat adaptations. *Nature* **583**, 578–
549 584 (2020).
550 44. Glaberman, S., Bulls, S. E., Vazquez, J. M., Chiari, Y. & Lynch, V. J. Concurrent evolution of
551 antiaging gene duplications and cellular phenotypes in long-lived turtles. *Genome Biol. Evol.* **13**,
552 evab244 (2021).

553 45. MacRae, S. L. *et al.* DNA Repair in Species with Extreme Lifespan Differences. *Aging* **7**, 1171–
554 1184 (2015).
555 46. Baines, C., Meitern, R., Kreitsberg, R. & Sepp, T. Comparative study of the evolution of cancer
556 gene duplications across fish. *Evol. Appl.* **15**, 1834–1845 (2022).
557 47. López-Otín, C., Blasco, M. A., Partridge, L., Serrano, M. & Kroemer, G. The Hallmarks of Aging.
558 *Cell* **153**, 1194–1217 (2013).
559 48. Moreno Santillán, D. D. *et al.* Large-scale genome sampling reveals unique immunity and
560 metabolic adaptations in bats. *Mol. Ecol.* **30**, 6449–6467 (2021).
561 49. Enard, D. & Petrov, D. A. Ancient RNA virus epidemics through the lens of recent adaptation in
562 human genomes. *Philos. Trans. R. Soc. Lond. B Biol. Sci.* **375**, 20190575 (2020).
563 50. Sotero-Caio, C. G., Baker, R. J. & Volleth, M. Chromosomal evolution in Chiroptera. *Genes (Basel)*
564 **8**, (2017).
565 51. Simão, F. A., Waterhouse, R. M., Ioannidis, P., Kriventseva, E. V. & Zdobnov, E. M. BUSCO:
566 assessing genome assembly and annotation completeness with single-copy orthologs.
567 *Bioinformatics* **31**, 3210–3212 (2015).
568 52. Manni, M., Berkeley, M. R., Seppey, M. & Zdobnov, E. M. BUSCO: assessing genomic data quality
569 and beyond. *Current Protocols* **1**, (2021).
570 53. Amador, L. I., Moyers Arévalo, R. L., Almeida, F. C., Catalano, S. A. & Giannini, N. P. Bat
571 Systematics in the Light of Unconstrained Analyses of a Comprehensive Molecular Supermatrix. *J.*
572 *Mamm. Evol.* **25**, 37–70 (2018).
573 54. Upham, N. S., Esselstyn, J. A. & Jetz, W. Inferring the mammal tree: Species-level sets of
574 phylogenies for questions in ecology, evolution, and conservation. *PLoS Biol.* **17**, e3000494
575 (2019).
576 55. Korstian, J. M., Paulat, N. S., Platt, R. N., Stevens, R. D. & Ray, D. A. SINE-Based Phylogenomics
577 Reveal Extensive Introgression and Incomplete Lineage Sorting in Myotis. *Genes* **13**, 399 (2022).
578 56. Foley, N. M. *et al.* Karyotypic stasis and swarming influenced the evolution of viral tolerance in a

579 species-rich bat radiation. *Cell Genom* **4**, 100482 (2024).
580 57. Volleth, M. Variations on a theme: Karyotype comparison in Eurasian Myotis species and
581 implications for phylogeny. *Vespertilio* **16**, 329–350 (2012).
582 58. McBee, K. Standard karyology of nine species of vespertilionid bats (Chiroptera: Vespertilionidae)
583 from Thailand. *Annals of Carnegie Museum* **55**, 95–116 (1986).
584 59. Bickham, J. W., McBee, K. & Schlitter, D. A. Chromosomal variation among seven species of
585 Myotis (Chiroptera: Vespertilionidae). *J. Mammal.* **67**, 746–750 (1986).
586 60. Zhang, W. D. A study on karyotype of Myotis chinensis and M. laniger Peter. *J Anhui Normal Univ*
587 **7**, 42–47 (1984).
588 61. Zima, J. Synopsis of karyotypes of vespertilionid bats (Mammalia: Chiroptera). *Acta Univ. Carol.*
589 *Biol* **1981**, 311–329 (1985).
590 62. O'Brien, S. J., Menninger, J. C. & Nash, W. G. *Atlas of Mammalian Chromosomes*. (John Wiley &
591 Sons, 2006).
592 63. Goel, M., Sun, H., Jiao, W.-B. & Schneeberger, K. SyRI: finding genomic rearrangements and local
593 sequence differences from whole-genome assemblies. *Genome Biol.* **20**, 277 (2019).
594 64. de Sotero-Caio, C. G. *et al.* Centromeric enrichment of LINE-1 retrotransposons and its
595 significance for the chromosome evolution of Phyllostomid bats. *Chromosome Res.* **25**, 313–325
596 (2017).
597 65. Morel, B., Kozlov, A. M., Stamatakis, A. & Szöllősi, G. J. GeneRax: A Tool for Species-Tree-Aware
598 Maximum Likelihood-Based Gene Family Tree Inference under Gene Duplication, Transfer, and
599 Loss. *Mol. Biol. Evol.* **37**, 2763–2774 (2020).
600 66. Kaufman, R. J. Double-stranded RNA-activated protein kinase mediates virus-induced apoptosis: a
601 new role for an old actor. *Proc. Natl. Acad. Sci. U. S. A.* **96**, 11693–11695 (1999).
602 67. García, M. A. *et al.* Impact of protein kinase PKR in cell biology: from antiviral to antiproliferative
603 action. *Microbiol. Mol. Biol. Rev.* **70**, 1032–1060 (2006).
604 68. Ostertag, D., Hoblitzell-Ostertag, T. M. & Perrault, J. Overproduction of double-stranded RNA in

605 vesicular stomatitis virus-infected cells activates a constitutive cell-type-specific antiviral response.
606 *J. Virol.* **81**, 503–513 (2007).
607 69. Enard, D., Cai, L., Gwennap, C. & Petrov, D. A. Viruses are a dominant driver of protein adaptation
608 in mammals. *Elife* **5**, (2016).
609 70. Murrell, B. *et al.* Gene-wide identification of episodic selection. *Mol. Biol. Evol.* **32**, 1365–1371
610 (2015).
611 71. Souilmi, Y. *et al.* An ancient viral epidemic involving host coronavirus interacting genes more than
612 20,000 years ago in East Asia. *Curr. Biol.* **31**, 3704 (2021).
613 72. Brook, C. E. & Dobson, A. P. Bats as 'special' reservoirs for emerging zoonotic pathogens. *Trends*
614 *Microbiol.* **23**, 172–180 (2015).
615 73. Kondrashov, F. A. Gene Dosage and Duplication. in *Evolution after Gene Duplication* (eds.
616 Dittmar, K. & Liberles, D.) 57–76 (John Wiley & Sons, 2011).
617 74. Kondrashov, F. A., Rogozin, I. B., Wolf, Y. I. & Koonin, E. V. Selection in the evolution of gene
618 duplications. *Genome Biol.* **3**, RESEARCH0008 (2002).
619 75. Rastogi, S. & Liberles, D. A. Subfunctionalization of duplicated genes as a transition state to
620 neofunctionalization. *BMC Evol. Biol.* **5**, 28 (2005).
621 76. Assis, R. & Bachtrog, D. Neofunctionalization of young duplicate genes in Drosophila. *Proc. Natl.*
622 *Acad. Sci. U. S. A.* **110**, 17409–17414 (2013).
623 77. Enard, D. & Petrov, D. A. Evidence that RNA Viruses Drove Adaptive Introgression between
624 Neanderthals and Modern Humans. *Cell* **175**, 360–371.e13 (2018).
625 78. Brunet-Rossinni, A. K. & Austad, S. N. Ageing studies on bats: a review. *Biogerontology* **5**, 211–
626 222 (2004).
627 79. Wilkinson, G. S. & South, J. M. Life History, Ecology and Longevity in Bats. *Aging Cell* **1**, 124–131
628 (2002).
629 80. Pyenson, N. D. & Sponberg, S. N. Reconstructing body size in extinct crown Cetacea (neoceti)
630 using allometry, phylogenetic methods and tests from the fossil record. *J. Mamm. Evol.* **18**, 269–

631 288 (2011).
632 81. Montgomery, S. H. *et al.* The evolutionary history of cetacean brain and body size: Cetacean brain
633 evolution. *Evolution* **67**, 3339–3353 (2013).
634 82. Puttick, M. N. & Thomas, G. H. Fossils and living taxa agree on patterns of body mass evolution: a
635 case study with Afrotheria. *Proc. Biol. Sci.* **282**, 20152023 (2015).
636 83. Sulak, M. *et al.* TP53 copy number expansion is associated with the evolution of increased body
637 size and an enhanced DNA damage response in elephants. *Elife* **5**, (2016).
638 84. Armitage, P. Multistage Models of Carcinogenesis. *Environ. Health Perspect.* **63**, 195–201 (1985).
639 85. Armitage, P. & Doll, R. The Age Distribution of Cancer and a Multi-Stage Theory of
640 Carcinogenesis. *Br. J. Cancer* **91**, 6602297 (2004).
641 86. Peto, R., Roe, F. J., Lee, P. N., Levy, L. & Clack, J. Cancer and ageing in mice and men. *Br. J.*
642 *Cancer* **32**, 411–426 (1975).
643 87. Peto, R. Quantitative Implications of the Approximate Irrelevance of Mammalian Body Size and
644 Lifespan to Lifelong Cancer Risk. *Philos. Trans. R. Soc. Lond. B Biol. Sci.* **370**, 20150198 (2015).
645 88. Nunney, L. Size Matters: Height, Cell Number and a Person's Risk of Cancer. *Proc. R. Soc. B* **285**,
646 20181743 (2018).
647 89. Caulin, A. F. & Maley, C. C. Peto's Paradox: evolution's prescription for cancer prevention. *Trends*
648 *Ecol. Evol.* **26**, 175–182 (2011).
649 90. Vincze, O. *et al.* Cancer risk across mammals. *Nature* **601**, 263–267 (2022).
650 91. Compton, Z. T. *et al.* Cancer prevalence across vertebrates. *Res. Sq.* (2023) doi:10.21203/rs.3.rs-
651 3117313/v1.
652 92. Tollis, M. *et al.* Return to the sea, get huge, beat cancer: An analysis of cetacean genomes
653 including an assembly for the humpback whale (Megaptera novaeangliae). *Mol. Biol. Evol.* **36**,
654 1746–1763 (2019).
655 93. Tollis, M., Schneider-Utaka, A. K. & Maley, C. C. The evolution of human cancer gene duplications
656 across mammals. *Mol. Biol. Evol.* **37**, 2875–2886 (2020).

657 94. Vazquez, J. M. *et al.* Parallel evolution of reduced cancer risk and tumor suppressor duplications in
658 Xenarthra. *Elife* **11**, e82558 (2022).
659 95. Caulin, A. F., Graham, T. A., Wang, L.-S. & Maley, C. C. Solutions to Peto's paradox revealed by
660 mathematical modelling and cross-species cancer gene analysis. *Philos. Trans. R. Soc. Lond. B*
661 *Biol. Sci.* **370**, 20140222 (2015).
662 96. Nair, N. U. *et al.* Cross-species identification of cancer resistance-associated genes that may
663 mediate human cancer risk. *Sci. Adv.* **8**, eabj7176 (2022).
664 97. Smith, M. D. *et al.* Less is more: an adaptive branch-site random effects model for efficient
665 detection of episodic diversifying selection. *Mol. Biol. Evol.* **32**, 1342–1353 (2015).
666 98. Hanahan, D. & Weinberg, R. A. Hallmarks of Cancer: The Next Generation. *Cell* **144**, 646–674
667 (2011).
668 99. Hanahan, D. & Weinberg, R. A. The Hallmarks of Cancer. *Cell* **100**, 57–70 (2000).
669 100. Hanahan, D. Hallmarks of Cancer: New Dimensions. *Cancer Discov.* **12**, 31–46 (2022).
670 101. Milacic, M. *et al.* The reactome pathway knowledgebase 2024. *Nucleic Acids Res.* **52**, D672–D678
671 (2024).
672 102. Abegglen, L. M. *et al.* Potential Mechanisms for Cancer Resistance in Elephants and Comparative
673 Cellular Response to DNA Damage in Humans. *JAMA* **314**, 1850–1860 (2015).
674 103. Firsanov, D. *et al.* DNA Repair and Anti-Cancer Mechanisms in the Longest-Living Mammal: The
675 Bowhead Whale. *bioRxiv* 2023.05.07.539748 (2023) doi:10.1101/2023.05.07.539748.
676 104. Lagunas-Rangel, F. A. Why do bats live so long?—Possible molecular mechanisms.
677 *Biogerontology* **21**, 1–11 (2020).
678 105. Chionh, Y. T. *et al.* High basal heat-shock protein expression in bats confers resistance to cellular
679 heat/oxidative stress. *Cell Stress Chaperones* **24**, 835–849 (2019).
680 106. Hua, R. *et al.* Experimental evidence for cancer resistance in a bat species. *Nat. Commun.* **15**,
681 1401 (2024).
682 107. Peixoto, F. P., Braga, P. H. P. & Mendes, P. A synthesis of ecological and evolutionary

683 determinants of bat diversity across spatial scales. *BMC Ecol.* **18**, 18 (2018).
684 108. USGS. North American Bat Ranges. (2022).
685 109. Rhie, A. *et al.* Towards complete and error-free genome assemblies of all vertebrate species.
686 *Nature* **592**, 737–746 (2021).
687 110. The Darwin Tree of Life Project Consortium. Sequence Locally, Think Globally: The Darwin Tree of
688 Life Project. *Proceedings of the National Academy of Sciences* **119**, e2115642118 (2022).
689 111. Lewin, H. A. *et al.* The Earth BioGenome Project 2020: Starting the Clock. *Proceedings of the*
690 *National Academy of Sciences* **119**, e2115635118 (2022).
691 112. Slater, G. J., Goldbogen, J. A. & Pyenson, N. D. Independent evolution of baleen whale gigantism
692 linked to Plio-Pleistocene ocean dynamics. *Proc. Biol. Sci.* **284**, (2017).
693 113. Tacutu, R. *et al.* Human Ageing Genomic Resources: new and updated databases. *Nucleic Acids*
694 *Res.* **46**, D1083–D1090 (2018).
695 114. Morales, A. E. *et al.* Bat genomes illuminate adaptations to viral tolerance and disease resistance.
696 *Nature* **638**, 449–458 (2025).
697 115. O'Shea, T. J. *et al.* Bat flight and zoonotic viruses. *Emerg. Infect. Dis.* **20**, 741–745 (2014).
698 116. Levesque, D. L., Boyles, J. G., Downs, C. J. & Breit, A. M. High Body Temperature is an Unlikely
699 Cause of High Viral Tolerance in Bats. *J. Wildl. Dis.* **57**, 238–241 (2021).
700 117. Kirkwood, T. B. L. The disposable soma theory. *The evolution of senescence in the tree of life* 23–
701 39 (2017).
702 118. Toshkova, N. *et al.* Temperature sensitivity of bat antibodies links metabolic state of bats with
703 antigen-recognition diversity. *Nat. Commun.* **15**, 5878 (2024).
704 119. Gutiérrez-Guerrero, Y. T. *et al.* Genomic consequences of dietary diversification and parallel
705 evolution due to nectarivory in leaf-nosed bats. *Gigascience* **9**, (2020).
706 120. Mandl, J. N., Schneider, C., Schneider, D. S. & Baker, M. L. Going to bat(s) for studies of disease
707 tolerance. *Front. Immunol.* **9**, 2112 (2018).
708 121. Pei, G., Balkema-Buschmann, A. & Dorhoi, A. Disease tolerance as immune defense strategy in

709 bats: One size fits all? *PLoS Pathog.* **20**, e1012471 (2024).
710 122. Vermillion, K. L., Anderson, K. J., Hampton, M. & Andrews, M. T. Gene expression changes
711 controlling distinct adaptations in the heart and skeletal muscle of a hibernating mammal. *Physiol.*
712 *Genomics* **47**, 58–74 (2015).
713 123. Lam, B. *et al.* Multi-species genome-wide CRISPR screens identify GPX4 as a conserved
714 suppressor of cold-induced cell death. *bioRxivorg* 2024.07.25.605098 (2024)
715 doi:10.1101/2024.07.25.605098.
716 124. Sone, M. & Yamaguchi, Y. Cold resistance of mammalian hibernators ~ a matter of ferroptosis?
717 *Front. Physiol.* **15**, 1377986 (2024).
718 125. Kaelber, J. T. *et al.* Evolutionary reconstructions of the transferrin receptor of Caniforms supports
719 canine parvovirus being a re-emerged and not a novel pathogen in dogs. *PLoS Pathog.* **8**,
720 e1002666 (2012).
721 126. Demogines, A., Abraham, J., Choe, H., Farzan, M. & Sawyer, S. L. Dual host-virus arms races
722 shape an essential housekeeping protein. *PLoS Biol.* **11**, e1001571 (2013).
723 127. Kerr, S. A. *et al.* Computational and functional analysis of the virus-receptor interface reveals host
724 range trade-offs in New World arenaviruses. *J. Virol.* **89**, 11643–11653 (2015).
725 128. Kaur, H. *et al.* Associations of L-Ferritin and Tim-1 with frailty measures in people with HIV: a
726 cross-sectional and longitudinal study. *Lancet Healthy Longev.* **3**, S5 (2022).
727 129. Kim, J., Jo, Y., Cho, D. & Ryu, D. L-threonine promotes healthspan by expediting ferritin-
728 dependent ferroptosis inhibition in C. elegans. *Nat. Commun.* **13**, 6554 (2022).
729 130. Daghlas, I. & Gill, D. Genetically predicted iron status and life expectancy. *Clin. Nutr.* **40**, 2456–
730 2459 (2021).
731 131. Perez, K. *et al.* Single nuclei profiling identifies cell specific markers of skeletal muscle aging,
732 frailty, and senescence. *Aging (Albany NY)* **14**, 9393–9422 (2022).
733 132. Trifunovic, A. *et al.* Premature ageing in mice expressing defective mitochondrial DNA polymerase.
734 *Nature* **429**, 417–423 (2004).

735 133. Van Goethem, G., Dermaut, B., Löfgren, A., Martin, J. J. & Van Broeckhoven, C. Mutation of POLG
736 is associated with progressive external ophthalmoplegia characterized by mtDNA deletions. *Nat.*
737 *Genet.* **28**, 211–212 (2001).
738 134. Cao, L., Li, W., Kim, S., Brodie, S. G. & Deng, C.-X. Senescence, aging, and malignant
739 transformation mediated by p53 in mice lacking the Brca1 full-length isoform. *Genes Dev.* **17**, 201–
740 213 (2003).
741 135. Vijg, J., Perls, T., Franceschi, C. & van Orsouw, N. J. BRCA1 gene sequence variation in
742 centenarians. *Ann. N. Y. Acad. Sci.* **928**, 85–96 (2001).
743 136. Fearon, E. R. Human cancer syndromes: clues to the origin and nature of cancer. *Science* **278**,
744 1043–1050 (1997).
745 137. Donoho, G. *et al.* Deletion of Brca2 exon 27 causes hypersensitivity to DNA crosslinks,
746 chromosomal instability, and reduced life span in mice. *Genes Chromosomes Cancer* **36**, 317–331
747 (2003).
748 138. Wooster, R. *et al.* Identification of the breast cancer susceptibility gene BRCA2. *Nature* **378**, 789–
749 792 (1995).
750 139. Ray, D. A. *et al.* Multiple Waves of Recent DNA Transposon Activity in the Bat, Myotis Lucifugus.
751 *Genome Res.* **18**, 717–728 (2008).
752 140. Sotgia, S. *et al.* Cellular immune activation in Sardinian middle-aged, older adults and
753 centenarians. *Exp. Gerontol.* **99**, 133–137 (2017).
754 141. Lee, K.-A., Flores, R. R., Jang, I. H., Saathoff, A. & Robbins, P. D. Immune senescence,
755 immunosenescence and aging. *Front. Aging* **3**, 900028 (2022).
756 142. Yousefzadeh, M. J. *et al.* An aged immune system drives senescence and ageing of solid organs.
757 *Nature* **594**, 100–105 (2021).
758 143. Lee, C.-S. *et al.* Upregulation of cluster of differentiation 36 mRNA expression in peripheral blood
759 mononuclear cells correlates with frailty severity in older adults. *J. Cachexia Sarcopenia Muscle*
760 **13**, 1948–1955 (2022).

761 144. Kimmel, J. C., Yi, N., Roy, M., Hendrickson, D. G. & Kelley, D. R. Differentiation reveals latent
762 features of aging and an energy barrier in murine myogenesis. *Cell Rep.* **35**, 109046 (2021).
763 145. Tian, Y. *et al.* FTH1 inhibits ferroptosis through ferritinophagy in the 6-OHDA model of Parkinson's
764 disease. *Neurotherapeutics* **17**, 1796–1812 (2020).
765 146. Ricklefs, R. E. Life-history connections to rates of aging in terrestrial vertebrates. *Proc. Natl. Acad.*
766 *Sci. U. S. A.* **107**, 10314–10319 (2010).
767 147. Tian, S. *et al.* Comparative analyses of bat genomes identify distinct evolution of immunity in Old
768 World fruit bats. *Sci Adv* **9**, eadd0141 (2023).
769 148. Jonathan Sleeman, Center Director, USGS National Wildlife Health Center. NWHC Operations
770 During the COVID-19 Pandemic and Information About Coronaviruses in Wildlife. (2020).
771 149. White-Nose Syndrome Disease Management Working Group. *National White-Nose Syndrome*
772 *Decontamination Protocol*. www.WhiteNoseSyndrome.org.
773 150. Wu, N. *et al.* The interferon stimulated gene 20 protein (ISG20) is an innate defense antiviral factor
774 that discriminates self versus non-self translation. *PLoS Pathog.* **15**, (2019).
775 151. Legrand, A. *et al.* SAMD9L acts as an antiviral factor against HIV-1 and primate lentiviruses by
776 restricting viral and cellular translation. *PLoS Biol.* **22**, e3002696 (2024).
777 152. Išerić, H., Alkan, C., Hach, F. & Numanagić, I. Fast characterization of segmental duplication
778 structure in multiple genome assemblies. *Algorithms Mol. Biol.* (2022).
779 153. Brown, M., González De la Rosa, P. M. & Mark, B. *A Telomere Identification Toolkit*. (2023).
780 doi:10.5281/zenodo.10091385.
781 154. Li, H. New strategies to improve minimap2 alignment accuracy. *Bioinformatics* (2021).
782 155. Goel, M. & Schneeberger, K. plotsr: visualizing structural similarities and rearrangements between
783 multiple genomes. *Bioinformatics* **38**, 2922–2926 (2022).
784 156. Minh, B. Q. *et al.* IQ-TREE 2: New Models and Efficient Methods for Phylogenetic Inference in the
785 Genomic Era. *Mol. Biol. Evol.* **37**, 1530–1534 (2020).
786 157. Zhang, C. & Mirarab, S. Weighting by gene tree uncertainty improves accuracy of quartet-based

787 species trees. *Mol. Biol. Evol.* **39**, (2022).
788 158. Romiguier, J., Ranwez, V., Delsuc, F., Galtier, N. & Douzery, E. J. P. Less is more in mammalian
789 phylogenomics: AT-rich genes minimize tree conflicts and unravel the root of placental mammals.
790 *Mol. Biol. Evol.* **30**, 2134–2144 (2013).
791 159. Foley, N. M. *et al.* A genomic timescale for placental mammal evolution. *Science* **380**, eabl8189
792 (2023).
793 160. Dos Reis, M. & Yang, Z. Bayesian Molecular Clock Dating Using Genome-Scale Datasets.
794 *Methods Mol. Biol.* **1910**, 309–330 (2019).
795 161. Yang, Z. PAML 4: phylogenetic analysis by maximum likelihood. *Mol. Biol. Evol.* **24**, 1586–1591
796 (2007).
797 162. Phillips, M. J. Geomolecular dating and the origin of placental mammals. *Syst. Biol.* **65**, 546–557
798 (2016).
799 163. Gunnell, G. F. & Simmons, N. B. Fossil evidence and the origin of bats. *J. Mamm. Evol.* **12**, 209–
800 246 (2005).
801 164. Eiting, T. P. & Gunnell, G. F. Global Completeness of the Bat Fossil Record. *J. Mamm. Evol.* **16**,
802 151–173 (2009).
803 165. Storch, G., Sigé, B. & Habersetzer, J. Tachypteron franzeni n. gen., n. sp., earliest emballonurid
804 bat from the Middle Eocene of Messel (Mammalia, Chiroptera). *Palaontol. Z.* **76**, 189–199 (2002).
805 166. Ravel, A. *et al.* A new large philisid (Mammalia, Chiroptera, Vespertilionoidea) from the late Early
806 Eocene of Chambi, Tunisia: LARGE BAT FROM CHAMBI. *Palaeontology* **55**, 1035–1041 (2012).
807 167. Lim, B. K. Review of the origins and biogeography of bats in South America. *Chiroptera*
808 *Neotropical* **15**, 391–410 (2009).
809 168. Morgan, G. S. & Czaplewski, N. J. A New Bat (Chiroptera: Natalidae) from the Early Miocene of
810 Florida, with Comments on Natalid Phylogeny. *J Mammal* **84**, 729–752 (2003).
811 169. Elliot, M. G. & Mooers, A. Ø. Inferring ancestral states without assuming neutrality or gradualism
812 using a stable model of continuous character evolution. *BMC Evol. Biol.* **14**, 226 (2014).

170. Kosakovsky Pond, S. L. *et al.* HyPhy 2.5-A customizable platform for evolutionary hypothesis testing using PHYlogenies. *Mol. Biol. Evol.* **37**, 295–299 (2020).

171. Mendes, F. K., Vanderpool, D., Fulton, B. & Hahn, M. W. CAFE 5 models variation in evolutionary rates among gene families. *Bioinformatics* **36**, 5516–5518 (2021).

Materials and Methods

Data availability

All sequencing data and genomes generated in this study are available on NCBI under Bioprojects PRJNA973719, PRJNA1035541, and PRJNA1295526. Annotations generated in this study are available at https://github.com/docmanny/myotis-gene-annotations. All other code is available at https://github.com/sudmantlab/MyotisGenomeAssembly. All other data are archived on DataDryad at DOI: 10.5061/dryad.02v6wwqfh.

Samples and materials

All bats sampled for this study were wild caught under scientific collection permits for California and Arizona (see Supplemental Table 1). Bats were sampled using standard mist-netting procedures, including taking standard body measurements, following USGS recommendations for White-Nose Syndrome and COVID-19 prevention[148,149]. For *M. lucifugus*, the donor individual was field-caught in California and transported to the Genetics Laboratory of the California Department of Fish and Wildlife, where they were euthanized via isofluorane. The *M. velifer* individual was caught in Arizona and euthanized in the field via isoflurane. For both *M. lucifugus* and *M. velifer*, tissues were collected and preserved via flash-freezing in liquid nitrogen. All other genomes were generated from primary cell lines. Additional information can be found in the *Extended Methods* and in **Table S1**.

All PKR experiments were performed using HeLa PKR-KO cells (kindly provided by A. Geballe, Fred Hutchinson Cancer Center, Seattle WA). The cells were maintained at 37°C with 5% CO_2 and cultured in DMEM supplemented with 5% fetal bovine serum (FBS), 1% penicillin/ streptomycin mix and 1 µg/mL puromycin (Sigma-Aldrich). All transfections were performed 24 hours after seeding, using 3 µL of TransIT-LT1 Transfection Reagent (Mirus Bio) per 1 µg of DNA and Opti-MEM media. We used previously-generated pSG5-FLAGx2 vectors encoding either *M. myotis* PKR1 (GenBank OP006550), *M. myotis* PKR2 (GenBank OP006559), *M. velifer* PKR1 (GenBank OP006558), or *M. velifer* PKR2 (GenBank OP006557)[28]. Plasmids encoding the interferon-stimulated gene ISG20[150] and a constitutively active variant of the sterile alpha motif domain-containing protein 9-like SAMD9L-F886Lfs*11 (here, SAMD9L[151]) were used as controls in viral infections and cell translation experiments, respectively.

Near-complete genome assembly and annotation

Details on DNA extraction, preparation of PacBio HiFi and Omni-C (Dovetail Genomics) libraries, and genome assembly and manual curation can be found in the *Extended Methods*.

Gene & repetitive element annotation and alignments

Details describing our procedure for identifying and annotation repetitive elements and protein-coding gene annotations can be found in the *Extended Methods.*

RNA sequencing for gene annotations and differential expression

Details on RNA extraction, library preparation, sequencing, and can be found in the *Extended Methods* and **Table S9**.

Structural variation

To understand the distribution of structural variants, including segmental duplication events, we used SyRI (Synteny and Rearrangement Identifier[63]) and BISER (Brisk Inference of Segmental duplication Evolutionary stRucture[152]). We first masked telomere regions using TIDK (Telomere Identification toolKit[153]), and mapped the primary 22 scaffolds of the nearctic *Myotis* genomes to each other with minimap2[154]. The scaffold corresponding to the X chromosome was omitted because there is no corresponding scaffold in the *M. yumanensis* assembly. To verify homologous chromosomes and fix strand orientation, we used *fixchr* from the SyRI package and manually renamed scaffolds accordingly, then re-mapped them with minimap2. We ran SyRI on the resulting files and plotted the results with plotsr[155]. We ran BISER on the primary 22 scaffolds of the nearctic *Myotis* genomes with –keep-contigs and default settings to generate bed files with the inferred segmental duplication regions.

Gene Trees & Phylogeny

A phylogeny of all 534 mammals in our alignments was generated using IQTREE[156] (version 2.3.1) using all gene alignments with the settings "-B 1000 -m GTR+F3x4+R6." To generate gene trees, we first filtered our gene alignments to exclude alignments with over 50% gaps in the sequence and less than 4 species. With the remaining alignments, we used IQTREE to find the best-fitting substitution model and tree using settings "--wbtl --bnni --alrt 1000 -B 1000 --safe". The best substitution models for each gene were saved as a NEXUS file. As the bootstrap values for this tree were unanimously 100%, we further confirmed the species tree by using ASTRAL-IV[157], and confirmed that our phylogeny agreed with other previously-published *Eutherian* phylogenies, including phylogenies of 39 mammals[158], of 241 placental mammals[159], and of 11 nearctic *Myotis* species[55].

Time-calibration of 59 bat genomes

Using our codon alignments of 59 bat genomes, we generated a time-calibrated phylogeny using mcmctree[160] and PAML[161] (v. 4.10.0) using an approximate likelihood method. Using the pan-bat codon alignments and our phylogeny as input, with fossil calibrations based on previously published work[4,43,159,162–168], we ran *mcmctree* twice to generate the Hessian matrix and confirm convergence. This was followed by 10 independent chains using the "out.BV" file from the first run. Finally, the output files of all 10 chains were combined to compute final divergence time estimates (see Table S2).

Ancestral Body Size, Lifespan, and Cancer Risk reconstruction

To explore how body size and lifespan have evolved over time in mammals, we used a super-phylogeny of mammal species[54] subsampled to only contain species with extant body size and lifespan data collected from AnAge[15] and PanTHERIA[16]. Ancestral body sizes and lifespans were simulated separately using StableTraits[169] and the settings "*--iterations 100000 --skip 1000 --chains 8*". Estimates were further validated by comparing our initial results to a second run of StableTraits using the same settings.

The Relative Incidence of Cancer Risk (RICR) was calculated across our mammalian phylogeny following the method of Vazquez and Lynch (2021)[37]. The cancer risk K for each node was calculated using the log of its median predicted body size and lifespan. An organism's lifetime risk of cancer K is proportional to Dt^6, where D is the body size and t is the maximum lifespan. RICR is then calculated as the $\log_2$ of the ratio between the cancer risk of a given node and its direct ancestor.

Selection Scans & Evolutionary Rates

aBSREL

To conservatively test for branch-specific selection, we used aBSREL[97,170] (version 2.5.48) to test for selection at each branch within the Nearctic *Myotis* clade for 15,734 gene alignments spanning 534 mammals. These genes were identified as 1:1 orthologs across the full alignment, with no more than 50% sequence gaps and at least 4 species present in the alignment. For each gene alignment, the full phylogeny was trimmed to match the species present, and the HYPHY script "label-tree.bf" was used to highlight all nodes within nearctic *Myotis* as foreground branches. aBSREL was then run using the pruned and highlighted tree and gene alignments on the command line with the options "--code Universal --branches Foreground". We defined a gene as under selection if one or more regions within the gene demonstrated a selective pressure with an FDR-corrected p-value ≤ 0.05; a gene was specifically identified as under positive selection if at least one of these significant regions had an $\omega>1$.

BUSTED

To quantify the total amount of positive selection across the *Myotis* tree or the different species trees used in this manuscript, we used an improved version of the BUSTED[70,170] test called BUSTED-MH (see *Extended Methods* for details on BUSTED vs BUSTED-MH). We applied BUSTED-MH to 19,646 *Myotis* orthologous CDS alignments with at least five orthologs. These orthologs are cases where the Orthofinder gene

908 trees coincide with the species tree. This effectively removes issues regarding whether we should use the gene
909 or the species tree, at the cost of removing 2,110 genes from the *Myotis* selection analysis. Similarly, we applied
910 BUSTED-MH to 17,469 non-*Myotis* bat alignments with at least five orthologs. The species in these two sets
911 (*Myotis* bats and non-*Myotis* bats) are mutually exclusive. This includes a subset of 14,091 alignments with
912 orthologs present in two thirds of the non-*Myotis* bat species, regardless of the genes' presence/absence in the
913 *Myotis*-only complement. This is specifically used to show that patterns of virus-driven adaptation are
914 representative of all bats. We also tested 17,890 primate alignments with at least five orthologs with BUSTED-
915 MH, as well as 19,311 glire, 18,000 carnivora and 18,504 ungulate alignments.

916 Enrichment scores for VIPs

917 We expanded on the set of VIPs reported in Souilmi *et al*. (2021)[71] (5,291 VIPs) by searching the literature
918 for more recent publications reporting VIPs, with a final dataset of 5,527 VIPs. These VIPs ("All VIPs") were
919 further sub-categorized into 4 groups based on their interactions with either DNA viruses and/or RNA viruses:
920 "DNA VIPs", "DNA-only VIPs", "RNA VIPs", and "RNA-only VIPs" (**Table S5**). For each VIP set, we selected sets
921 of matching control genes by controlling for 16 different criteria. (Table S5). Sets of control genes were resampled
922 in a bootstrap procedure to generate 95% confidence intervals for sets of genes across a range of p-values;
923 additional details can be found in the *Extended Methods*.

924 Gene Duplications and CAFE analysis

925 To quantify patterns of gene duplication and loss, we quantified the copy number of genes with human
926 orthologs from our gene annotations for each nearctic *Myotis* genome. To calculate per-gene expansion and
927 loss rates and their statistical significance, we ran CAFE[171] v5 on the previously described set of copy number
928 counts using our time-calibrated species tree pruned to include only the nine nearctic *Myotis* species. CAFE
929 uses a birth-death model of gene family evolution to investigate changes in gene family size accounting for
930 evolutionary history using the species phylogeny. Evolutionary branch length is incorporated into the model
931 expectations, thus accounting for potential bias resulting from differences in branch lengths. We ran CAFE on
932 the subset of genes with two or more copies in at least one species using a Poisson distribution for the root
933 frequency (*-p*), first generating an error model to correct for genome assembly and annotation error (*-e*). We
934 compared the base model (each gene family belongs to the same evolutionary rate category) to gamma models
935 (each gene family can belong to one of *k* evolutionary rate categories) with different values of *k* from 2 to 13. A
936 final gamma model with *k*=9 was chosen to balance model log likelihood with the number of gene families for
937 which the optimizer failed. The model was run three separate times to ensure convergence.

938 To understand if genes in these pathways have higher birth rates or are more likely to have significant
939 changes in gene copy number than expected relative to other genes, we evaluated the gene copy birth rate λ
940 and number of genes that have significantly expanded or contracted in copy number on at least one branch
941 within our nearctic *Myotis* phylogeny using a bootstrap procedure. Following Huang et al.[41], we tested if VIP
942 genes in particular underwent significant copy number changes or had significantly different birth/death rates
943 than non-VIP genes. For each category of VIP genes (all VIPs, DNA VIPs, DNA only VIPs, RNA VIPs, and RNA
944 only VIPs), we generated 100 bootstrap sets of control non-VIP genes with the same number of genes as the
945 corresponding VIP gene set. We ran CAFE on each set of VIP genes and the corresponding control non-VIP
946 genes to infer per-gene birth-death rates and per-gene, per-branch expansion/loss events.

947 # Assessment of DNA Double-Strand Break Tolerance

948 We assessed each species' tolerance to DNA double strand breaks using a by measuring viability,
949 cytotoxicty, and apoptosis across a range of doses of Neocarzinostatin, a radiomimetic drug. We measured dose
950 response curves in wing-derived primary dermal fibroblasts across 5 bat species (*Myotis lucifugus*, n=8; *Myotis*
951 *evotis*, n=8; *Rousettus langosus*, n=2; *Eidolon helvum*, n=2; *Pteropus rodrigensis*, n=2) using the multiplexed
952 ApoTox-Glo assay (Promega). Using 96-well plates, two individuals and 11 doses were assessed simultaneously
953 with four technical replicates. Results were normalized to treatment controls for each individual in R as previously
954 described[35,36,39,44].

955 # PKR1/2 Characterization in PKR-KO HeLa cells

956 ## Western blot

957 We assessed for the steady state protein expression of *M. myotis* Flag-PKRs after transfection of 350 ng
958 or 700 ng total of DNA plasmids encoding: PKR1 alone, PKR2 alone or both PKR1 and PKR2 (175 ng of each
959 and 350 ng of each, respectively). Briefly, cells were re-suspended and lysed in ice-cold RIPA buffer (50 mM
960 Tris pH8, 150 mM NaCl, 2 mM EDTA, 0.5% NP40) with protease inhibitor cocktail (Roche) and sonicated. 20 µL
961 of the clarified fraction was denatured with 5 µL of 6x Laemmli buffer at 95°C for 5 min and loaded into 4-20%
962 BioRad Criterion TGX Stain-Free precast gel. The wet transfer into a PVDF membrane was executed overnight
963 at 4°C. The membranes were blocked in a 1xTBS-T buffer (Tris HCl 50 mM pH8, NaCl 30 mM, 0.05% of Tween
964 20) containing 10 % powder milk, and were incubated for 1h. The membranes were incubated with primary
965 mouse anti-Flag (Sigma F3165) and anti-Tubulin (Sigma T5168) antibodies and secondary anti-Mouse IgG-
966 Peroxidase conjugated (Sigma A9044). Detection was made using the Chemidoc Imaging System (BioRad) with
967 SuperSignal West Pico Chemiluminescent Substrate (ThermoFisher Scientific).

968 ## Luciferase reporter assays

969 Luciferase reporter assays were carried out to investigate whether the two PKR paralogs have
970 synergistic, additive or dominant negative effect in translation shutdown. 25,000 PKR-KO cells were seeded in
971 24-well plates. The next day, cells were transfected with 350 ng of empty pSG5, 350 ng of PKR1, 350 ng of
972 PKR2, or 175 ng of PKR1+ 175 ng of PKR2, with additional 50 ng of FFLuc firefly luciferase reporter plasmid per
973 well. Sterile alpha motif domain-containing proteins 9L (SAMD9L gain-of-function mutant) was used as a positive
974 control of translational repression[151]. 24 h post transfection, cells were washed with PBS, lysed by a 5× reporter
975 lysis buffer (Promega) and incubated overnight at -20°C. Cells were then collected and 100 µl of the luciferase
976 substrate (Promega) was added to 20 µl of the lysis supernatant. Alternatively, cells were lysed using BrightGlow
977 Lysis Reagent (Promega E2620). The relative luminescence units (RLUs) proportional to the translation of the
978 luciferase reporter were immediately quantified with LUMIstar Omega microplate reader optima (BMG Labtech).
979 All luciferase assays were conducted in technical duplicates in at least five independent experiments. Fold
980 change results were normalized to the empty pSG5 condition within each independent experiment.

981 ## PKR co-immunoprecipitation

982 Hela PKR-KO cells were transfected with 1.25µg plenti6 HA-tagged *M. myotis* PKR1 plasmid per million cells
983 and 1.25µg of either plenti6 myc empty vector, myc-tagged *M. myotis* PKR1 or myc-tagged *M. myotis* PKR2
984 plasmid using TransIT-LTI transfection reagent (Mirus Bio). The next day, some wells were infected with Sindbis

985 virus expressing GFP (SINV-GFP) at MOI 2 for 24 hours. Cells were then scraped with cold PBS and pelleted.
986 For the IP, cells were lysed in 500µl IP buffer (50mM Tris HCl pH7.5, 140mM NaCl, 6 mM MgCl2, 0.1% NP40)
987 supplemented with RNase (RiboLock, Fisher Scientific) and protease (complete EDTA-free protease inhibitor
988 cocktail, Sigma) inhibitors for 10 minutes on ice, then centrifuged at 12,000 *xg* for 10 min at 4°C. 5% of the
989 volume was kept for input, while the rest was incubated with 40µl µMACS anti-c-myc MicroBeads (Miltenyi
990 Biotec) for 1h at 4°C with constant rotation. Samples were then loaded onto µMACS columns placed in the
991 magnetic field of a µMACS Separator (Miltenyi Biotec), washed 4 times with cold IP buffer, and eluted with the
992 µMACS denaturing elution buffer. Proteins were denatured in elution buffer for 5 min at 95°C, then loaded onto
993 a 4-20% BioRad Criterion TGX Stain-Free precast gel and transferred onto an Amersham Protran nitrocellulose
994 membrane (Sigma) for 1h. Membranes were blocked for 1h in 5% milk in PBS (Euromedex) supplemented with
995 0.2% tween (Fisher) and incubated with mouse anti-myc monoclonal antibodies (Abcam 9E10, cat# ab32) then
996 secondary anti-mouse IgG antibodies conjugated with HRP (Sigma, cat# A4416), or with rat anti-HA antibodies
997 conjugated with HRP (Roche, Sigma, cat# 12013819001). Images were taken on a Fusion FX imager (Vilber)
998 with SuperSignal West Femto Chemiluminescent Substrate (ThermoFisher Scientific).

999 Cell viability assay

1000 Hela PKR-KO cells were transfected 24h after plating in 96 well plates (n=10,000 cells/well), with 100 or
1001 200 ng of pSG5 plasmid: empty or coding for *M. myotis* or *M. velifer* PKR1, PKR2 or PKR1+2 equal mix (50%-
1002 50%). 24 hours post-transfection, positive control cells were treated with an apoptosis-inducing drug, Etoposide,
1003 at different doses (250, 200 or 100 µM). 48 hours post transfection, cells were harvested and lysed to quantify
1004 luminescent signal according to CellTiter-Glo® Luminescent Cell Viability Assay (Promega) kit protocol.

1005 VSV and SINV infections

1006 VSV infections. 200,000 cells were plated in 12-well and transfected 24 h after with 350 ng of pSG5
1007 plasmid: empty, or encoding *M. myotis* or *M. velifer* PKR1, PKR2, or equal input of PKR1 and PKR2 (175 ng per
1008 plasmid), or a plasmid encoding interferon-stimulated exonuclease gene 20 (ISG20), due to its known antiviral
1009 activity against VSV as positive control[150]. Cells were infected 24 h post transfection with replicative VSV-GFP
1010 virus[68] at a MOI of 3. Cells were fixed with 4% paraformaldehyde 16-18 hours post infection. VSV infection was
1011 quantified by measuring the percentage of GFP positive cell populations with BD FACSCanto II Flow Cytometer
1012 (SFR BioSciences). Fold change results were normalized to the empty pSG5 condition across at least three
1013 independent experiments.

1014 SINV infections. Hela PKR-KO cells were transfected with 5µg pSG5 empty vector, *M. myotis* PKR1, *M.*
1015 *myotis* PKR2 or 2.5µg *M. myotis* PKR1 + 2.5µg *M. myotis* PKR2 per million cells using TransIT-LTI transfection
1016 reagent (Mirus Bio). The next day, some wells were infected with SINV-GFP at MOI 0.2. Cells were then placed
1017 into a CellCyte X live cell imaging system (Cytena) and pictures of every well were taken every 2h for 48h. The
1018 fraction of GFP+ cells over the total cell area was measured and averaged from six photos of 2 individual wells
1019 per condition, and repeated for a total of three independent experiments.

Fig. Legends

Fig. 1: 8 near-complete reference assemblies for North American (Nearctic) *Myotis*. A) Phylogeny of 38 bat genomes with 3 outgroup species: cow *(bosTau9*), mouse (*mm39*); and human (*T2T-CHM13v2.0*). Bars at the tips of the phylogeny indicate the Area under the NGx curve (AuNG) score of each genome, a metric of genome contiguity independent of genome size. The dotted line represents the AuNG score for the T2T-CHM13v2.0 assembly. **B)** The time-calibrated phylogeny of 9 Nearctic and two representative Palaearctic *Myotis* species based on orthologous codon alignments. Blue bars represent age uncertainties. **C)** Map of capture sites for new cell lines with representative images for the species sequenced in this study (see "Acknowledgements" for attributions). **D)** Mammalian BUSCO scores for annotations generated for the 8 new *Myotis* genomes. **E)** Ideogram bar plot indicating completion status of each chromosome in assembly. Pie graphs indicate completion status of all chromosomes in assembly. Percentages above ideogram indicate the proportion of T2T assembled chromosomes across species. All chromosomes were positively identified based on size, synteny, and homology to human chromosomes[50]. "Complete (T2T)" status indicates that a chromosome is fully assembled telomere-to-telomere without gaps; "Draft (T2T, gaps)" status indicates that a chromosome is fully scaffolded with both telomeres, but has one or more gaps in the assembly; "Incomplete" status indicates that a chromosome was positively identified, but was not scaffolded from telomere to telomere (only contains one telomere).

Fig. 2: A varied structural variation landscape across 9 nearctic *Myotis* species. A) Synteny between chromosomes of 9 *Myotis* species showing syntenic regions (grey), inversions (orange), translocations (green), and duplications (blue). **B)** Distribution of transposable elements (top) and segmental duplications (red heatmap, bottom) in *M. velifer*. Putative locations of centromeres are denoted by the dotted lines. **C)** Pie chart of overall genomic proportions of TEs in *M. velifer*. **D)** Histogram of segmental duplication size distributions genome-wide in *M. velifer*.

Fig. 3: Evolutionary history and function of an actively segregating copy number polymorphism of *PKR* in *Myotis*. A) Structural comparison of the main PKR haplotypes in two species. Orthologous regions between the two haplotypes are indicated by grey bands, while syntenic duplications are indicated in green. Exons are annotated with black marks. **B)** Cartoon of the PKR locus in the two phased haplotype assemblies of each species. While *PKR2* is present across all haplotypes, *PKR1* and *PKR copy 3* are polymorphic within and across species. Each number indicates the number of exons per gene. **C)** Reconciled gene tree for *PKRs* across all haplotypes and species shown in B. Haplotype corresponding to the reference (A) and alternate (B) haplotype for each species are represented by upper- and lower-diagonal triangles, respectively. **D)** Effect of Myotis PKR expression on luciferase reporter translation in PKR-KO cells, measured in Relative Light Units (RLU) and normalized to the empty pSG5 control. Human SAMD9L-GoF is a positive control of translation inhibition[151]. **E-F)** Effect of PKR on viral infection by VSV-GFP (E, and S3B) and SINV-GFP (F 34h post-infection, and S3C), measured by flow cytometry as the % of GFP+ cells, normalized to the pSG5 control. Although all conditions restricted VSV and SINV, the expression of both PKR1+PKR2 was not beneficial against these viral infections. ISG20 served as a positive control of VSV-GFP restriction[150]. **G)** Co-immunoprecipitation (IP) of PKR-KO cells transfected with *Myotis* HA-PKR1 and either *Myotis* myc-PKR1, *Myotis* myc-PKR2 or a myc-empty vector control. Proteins were pulled down with anti-myc beads and lysates from 5% input or IP samples were run on a western blot and stained for HA and myc. Representative of 3 independent experiments. Extended Data Fig. 3E for SINV conditions. H, Quantification of the three independent experiments (mock and SINV): HA left and myc right. For **D-F**, error bars indicate the means ± SEM for at least three independent experiments. Statistics, unpaired t-test ($p<0.05$). mPKR, Myotis myotis PKR; vPKR, Myotis velifer PKR.

Fig. 4: Adaptation to DNA viruses, but not RNA viruses, is enriched in *Myotis* and other bats. A) Diagram of an example VIP, host cell transmembrane receptor CD45, showing strength of adaptation at each codon and the locations of direct interactions with the human adenovirus protein sec49K. **B-F)** Enrichment plots showing the ratio

of positive selection in only *Myotis* bats in VIPs versus matched sets of control genes at different p-value thresholds. The solid line shows the median ratio; the color of the line, and the number above each point, represents the number of VIPs with significant BUSTED-MH p-values at the given threshold; the grey band represents the 95% confidence interval generated by bootstrapping sets of matched control genes. The 95% confidence interval widens at lower p-values because there are fewer VIPs with significant p-values as the alpha threshold decreases, reducing power. **G-I)** The same as above, across all bats in this study excluding *Myotis*. **J-L)** The number of VIP genes inferred by CAFE to have significantly expanded or contracted in copy number on at least one branch of the nearctic *Myotis* phylogeny (blue line) compared to the distribution across 100 randomized sets of non-VIP control genes (black line). Vertical dashed lines indicated the 95% highest density interval for the control gene distribution.

Fig. 5: Evolution of cancer risk and resistance in *Myotis* and other mammals. A, B) Cophylo plot of the evolution of body size (**A**) and lifespan (**B**) across *Eutheria*. Branch lengths in **A-B** are scaled proportional to the rate of change of the trait over time. **C)** Diagram illustrating the relationship between changes in body size and lifespan with changes in cancer risk and resistance. **D)** Relative Intrinsic Cancer Risk (RICR) for every node in *Eutheria*, ranked from greatest reduction in cancer risk to greatest increase in cancer risk. RICR relative to the most recent ancestor of select nodes are highlighted, as well as the average RICR across for all nodes within select clades. **E)** The phylogeny of Nearctic *Myotis* species with inset pie charts representing the proportion of the top 100 Reactome pathways overrepresented among genes under selection at each node that are associated with cancer-related processes. Below, pie chart indicates expected proportion of pathways are cancer-associated after 1000 random samples of 100 pathways from the full Reactome database. Asterisks represent nodes with proportions greater than the expected value at $p \leq 0.05$ using Fisher's exact test. **F)** Proportion of the top 100 Reactome pathways overrepresented among genes under selection across all nodes in a species' evolutionary history that are associated with cancer-related processes. **G)** Volcano plot of overrepresented pathways in Reactome among the union set of genes under selection across all nodes in the evolutionary history for *M. lucifugus*. **H)** Viability and Apoptosis fold-change in 5 bat species in response to different doses of neocarzinostatin (NCS), a potent inducer of DNA double-strand breaks. Points represent individual replicates normalized to each species' control, while bars represent mean ± 95% confidence intervals.

Fig. 6: **Pleiotropy among genes under selection in *M. lucifugus* between DNA-damage responsive genes and DNA-only VIPs. A-B)** Volcano plots of genes that are differentially expressed in *M. lucifugus* after 6 hours (**A**) and 18 hours (**B**) of treatment with 100uM neocarzinostatin (NCS). **C-D)** Pathway-level Gene Set Enrichment Analysis (GSEA) of genes differentially expressed at 6 and 18 hours post-treatment. **E)** Upset plot between genes that are differentially expressed after NCS treatment and DNA-only VIPs; the hypergeometric P-value of the intersection is shown. **F)** Pathway-level overrepresentation analysis of genes that are DNA-only VIPs and are also differentially expressed in response to NCS treatment. **G)** Pathway-level overrepresentation analysis of genes identified as under selection in *M. lucifugus* via ABSREL that are DNA-only VIPs and are also differentially expressed in response to NCS treatment.

Supplemental Information

Extended Data Fig. 1-7:

1. **Contiguity statistics for 8 novel *Myotis* genomes**
2. **Estimated node divergence times for *Chiroptera* and ASTRAL-IV scores.**
3. **Correlations of TEs and structural variation in *Myotis* genomes**
4. **Additional functional characterization of *Myotis* PKR duplicates**
5. **VIP selection enrichments in bats and other mammals**
6. **Evolution of Cancer Risk and Resistance across *Myotis***
7. **Genes differentially expressed after neocarzinostatin treatment and their overlap with DNA-only VIPs**

Table S1. Genome Statistics
Table S2. Accessions for additional genomes used in this study
Table S3. SyRI-identified structural variants (SVs)
Table S4. Experimental data for PKR experiments
Table S5. List of VIPs and VIP subclasses
Table S6. Ancestral State Reconstructions for body size, lifespan, and RICR in mammals
Table S7. aBSREL significant gene lists and Reactome enrichments
Table S8. Experimental data for Neocarzinostatin experiments
Table S9. RNA-seq QC statistics and GSEA results

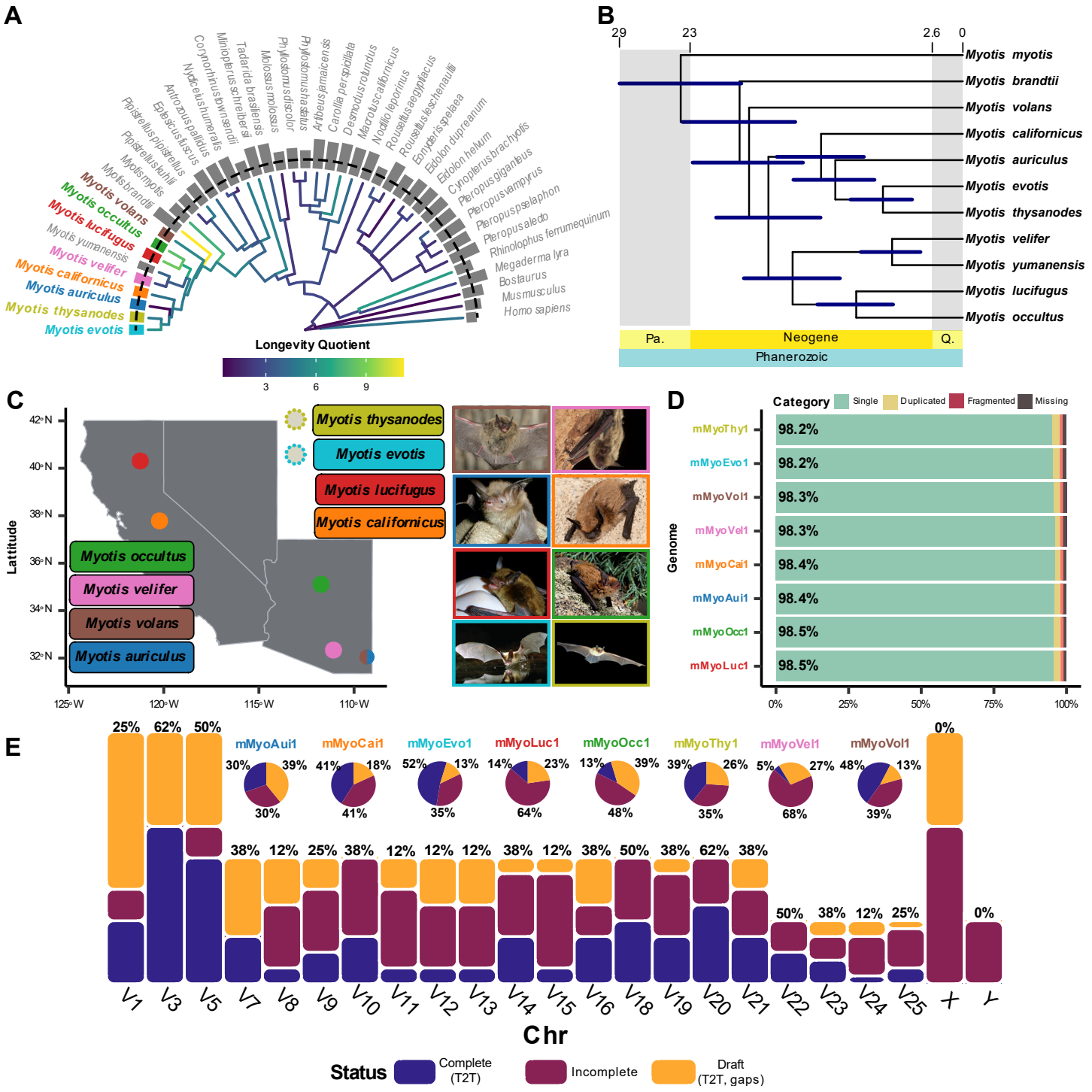
A
Longevity Quotient
3
6
9
Myotis volans
Myotis occultus
Myotis lucifugus
Myotis yumanensis
Myotis velifer
Myotis californicus
Myotis auriculus
Myotis thysanodes
Myotis evotis
Homo sapiens
B
29
23
2.6
0
Myotis myotis
Myotis brandtii
Myotis volans
Myotis californicus
Myotis auriculus
Myotis evotis
Myotis thysanodes
Myotis velifer
Myotis yumanensis
Myotis lucifugus
Myotis occultus
Pa.
Neogene
Q.
Phanerozoic
C
Lattitude
42°N
40°N
38°N
36°N
34°N
32°N
125°W
120°W
115°W
110°W
Myotis thysanodes
Myotis evotis
Myotis lucifugus
Myotis californicus
Myotis occultus
Myotis velifer
Myotis volans
Myotis auriculus
D
Category
Single
Duplicated
Fragmented
Missing
Genome
mMyoThy1
mMyoEvo1
mMyoVol1
mMyoVel1
mMyoCai1
mMyoAui1
mMyoOcc1
mMyoLuc1
98.2%
98.2%
98.3%
98.3%
98.4%
98.4%
98.5%
98.5%
0%
25%
50%
75%
100%
E
mMyoAui1
mMyoCai1
mMyoEvo1
mMyoLuc1
mMyoOcc1
mMyoThy1
mMyoVel1
mMyoVol1
Chr
Status
Complete (T2T)
Incomplete
Draft (T2T, gaps)

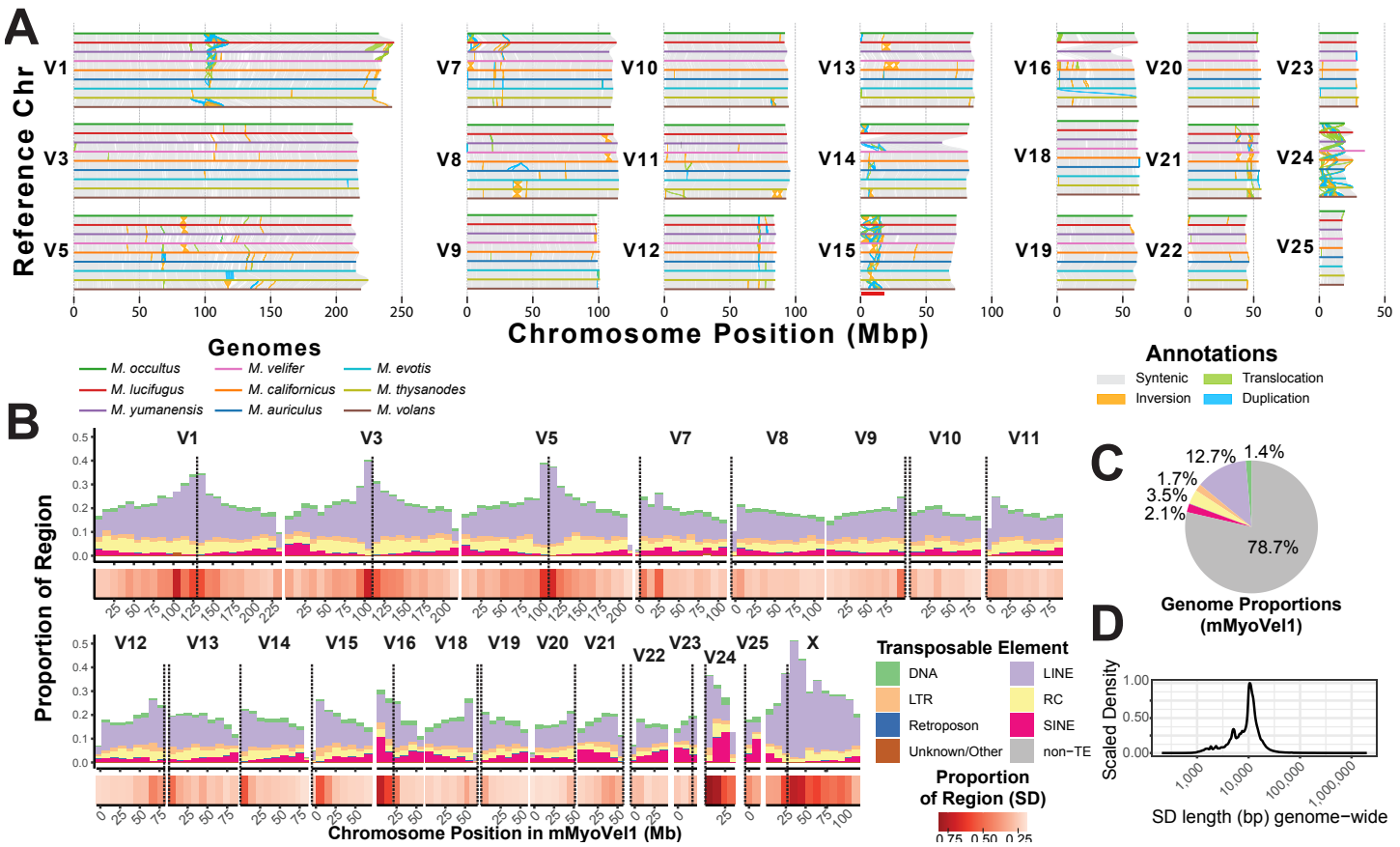
A
Reference Chr
V1
V3
V5
V7
V8
V9
V10
V11
V12
V13
V14
V15
V16
V18
V19
V20
V21
V22
V23
V24
V25
Chromosome Position (Mbp)
Genomes
M. occultus
M. lucifugus
M. yumanensis
M. velifer
M. californicus
M. auriculus
M. evotis
M. thysanodes
M. volans
Annotations
Syntenic
Inversion
Translocation
Duplication
B
Proportion of Region
X
Chromosome Position in mMyoVel1 (Mb)
Transposable Element
DNA
LTR
Retroposon
Unknown/Other
LINE
RC
SINE
non−TE
Proportion of Region (SD)
C
12.7%
1.4%
1.7%
3.5%
2.1%
78.7%
Genome Proportions (mMyoVel1)
D
Scaled Density
SD length (bp) genome−wide

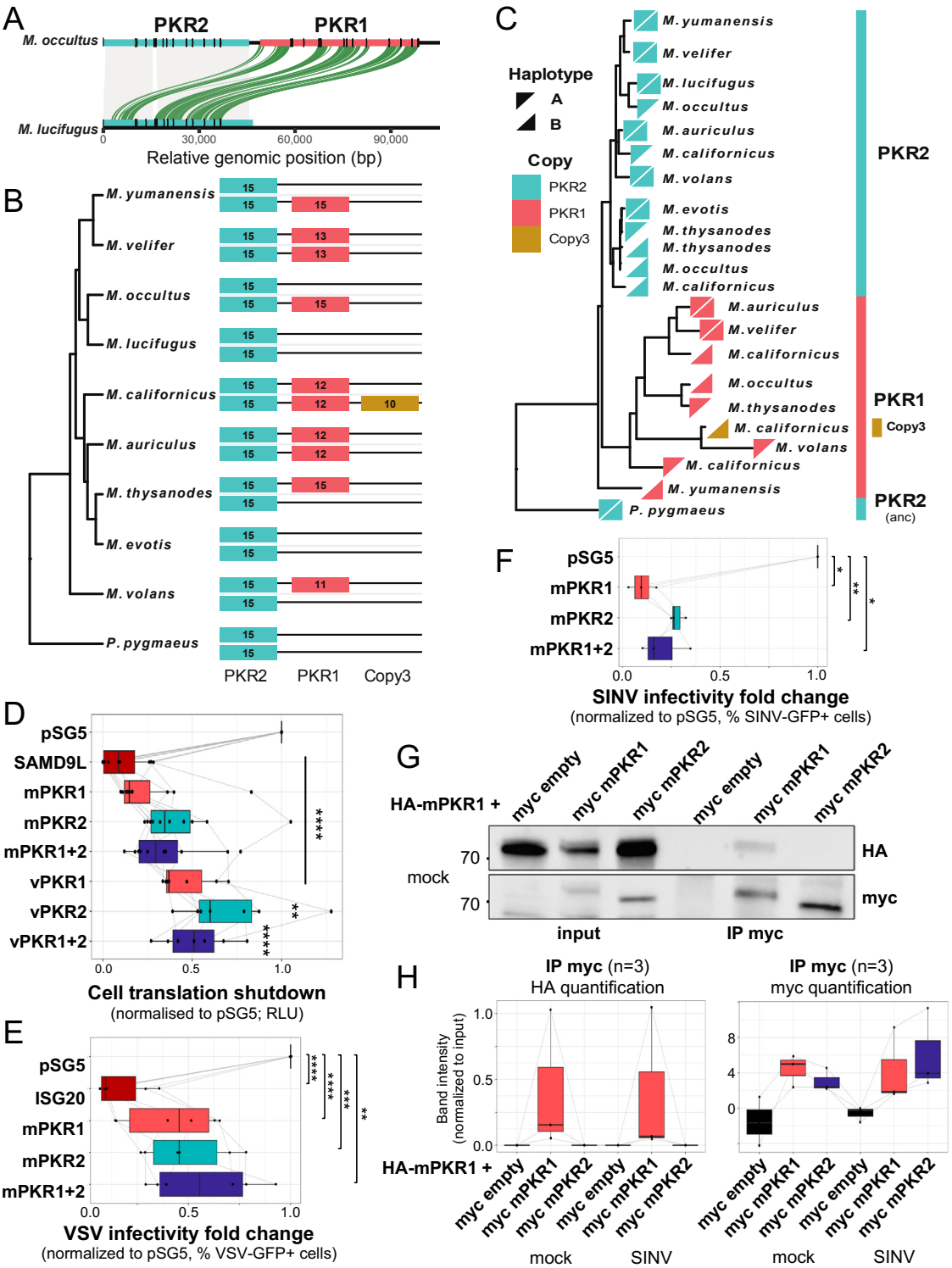
A
PKR2
PKR1
M. occultus
M. lucifugus
0
30,000
60,000
90,000
Relative genomic position (bp)
B
M. yumanensis
M. velifer
M. occultus
M. lucifugus
M. californicus
M. auriculus
M. thysanodes
M. evotis
M. volans
P. pygmaeus
PKR2
PKR1
Copy3
C
Haplotype
A
B
Copy
PKR2
PKR1
Copy3
M. yumanensis
M. velifer
M. lucifugus
M. occultus
M. auriculus
M. californicus
M. volans
M. evotis
M. thysanodes
M. thysanodes
M. occultus
M. californicus
M. auriculus
M. velifer
M. californicus
M. occultus
M. thysanodes
M. californicus
M. volans
M. californicus
M. yumanensis
P. pygmaeus
PKR2
PKR1
Copy3
PKR2
(anc)
D
pSG5
SAMD9L
mPKR1
mPKR2
mPKR1+2
vPKR1
vPKR2
vPKR1+2
Cell translation shutdown
(normalised to pSG5; RLU)
E
pSG5
ISG20
mPKR1
mPKR2
mPKR1+2
VSV infectivity fold change
(normalized to pSG5, % VSV-GFP+ cells)
F
pSG5
mPKR1
mPKR2
mPKR1+2
SINV infectivity fold change
(normalized to pSG5, % SINV-GFP+ cells)
G
HA-mPKR1 +
myc empty
myc mPKR1
myc mPKR2
mock
70
HA
myc
input
IP myc
H
IP myc (n=3)
HA quantification
Band intensity
(normalized to input)
IP myc (n=3)
myc quantification
HA-mPKR1 +
mock
SINV

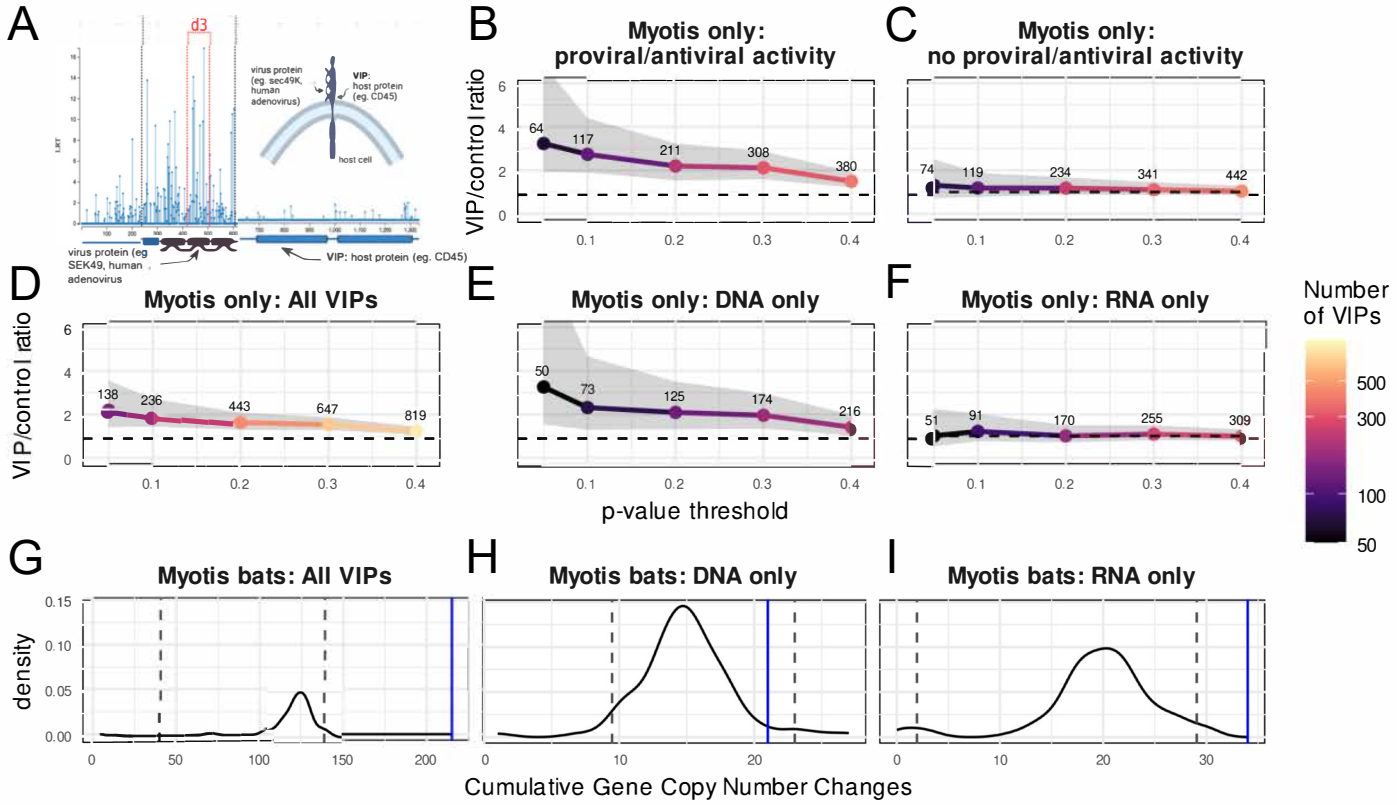
A
d3
virus protein (eg. sec49K, human adenovirus)
VIP: host protein (eg. CD45)
host cell
virus protein (eg SEK49, human adenovirus
VIP: host protein (eg. CD45)
B
Myotis only: proviral/antiviral activity
VIP/control ratio
64
117
211
308
380
C
Myotis only: no proviral/antiviral activity
74
119
234
341
442
D
Myotis only: All VIPs
138
236
443
647
819
E
Myotis only: DNA only
50
73
125
174
216
F
Myotis only: RNA only
51
91
170
255
309
p-value threshold
Number of VIPs
500
300
100
50
G
Myotis bats: All VIPs
density
H
Myotis bats: DNA only
I
Myotis bats: RNA only
Cumulative Gene Copy Number Changes

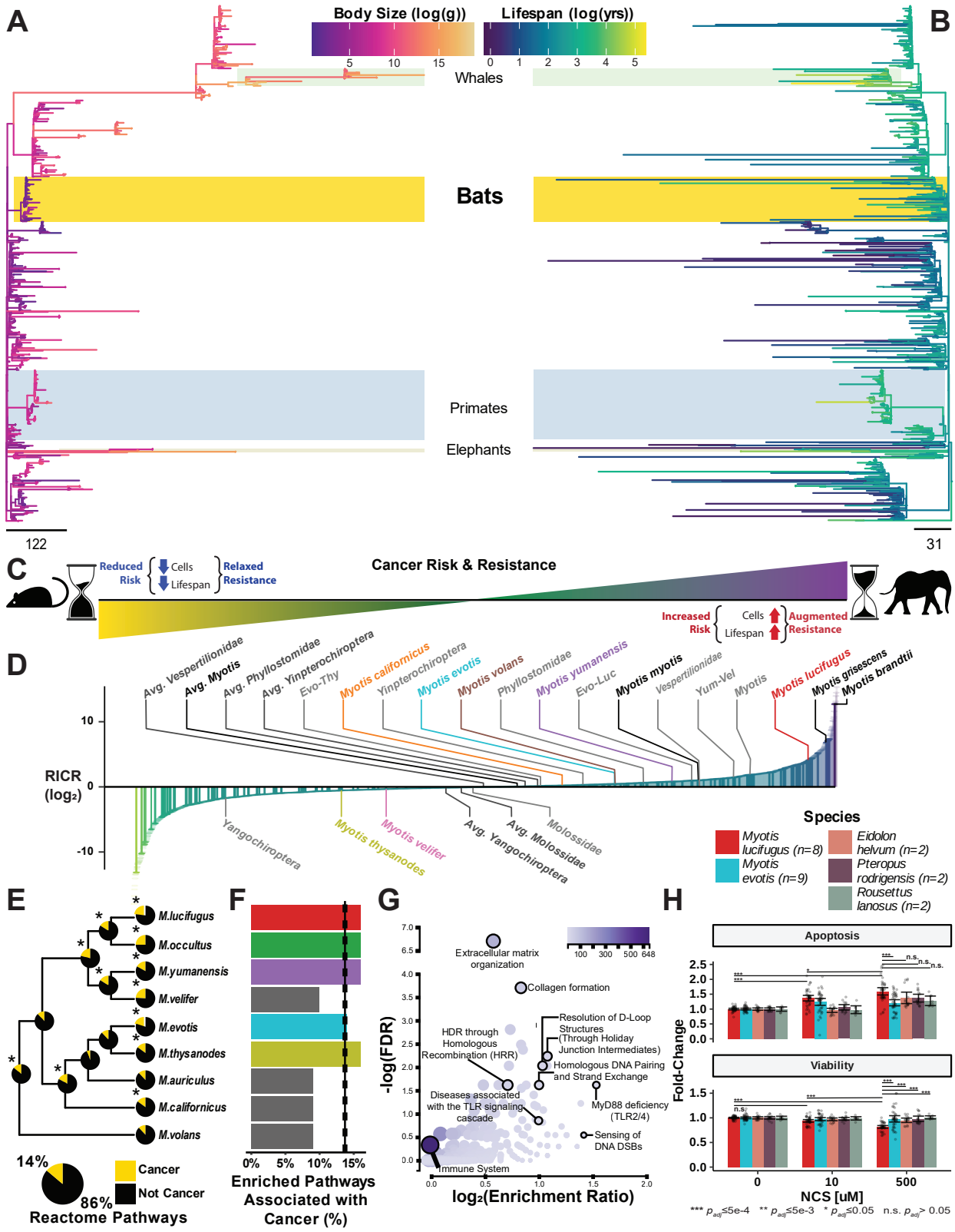
A
B
Body Size (log(g))
5
10
15
Lifespan (log(yrs))
0
1
2
3
4
5
Whales
Bats
Primates
Elephants
122
31
C
Reduced Risk
Cells
Lifespan
Relaxed Resistance
Cancer Risk & Resistance
Increased Risk
Cells
Lifespan
Augmented Resistance
D
Avg. Vespertilionidae
Avg. Myotis
Avg. Phyllostomidae
Avg. Yinpterochiroptera
Evo-Thy
Myotis californicus
Yinpterochiroptera
Myotis evotis
Myotis volans
Phyllostomidae
Myotis yumanensis
Evo-Luc
Myotis myotis
Vespertilionidae
Yum-Vel
Myotis
Myotis lucifugus
Myotis grisescens
Myotis brandtii
RICR (log2)
10
0
-10
Yangochiroptera
Myotis thysanodes
Myotis velifer
Avg. Yangochiroptera
Avg. Molossidae
Molossidae
Species
Myotis lucifugus (n=8)
Myotis evotis (n=9)
Eidolon helvum (n=2)
Pteropus rodrigensis (n=2)
Rousettus lanosus (n=2)
E
M.lucifugus
M.occultus
M.yumanensis
M.velifer
M.evotis
M.thysanodes
M.auriculus
M.californicus
M.volans
14%
86%
Cancer
Not Cancer
Reactome Pathways
F
0%
5%
10%
15%
Enriched Pathways Associated with Cancer (%)
G
Extracellular matrix organization
Collagen formation
Resolution of D-Loop Structures (Through Holiday Junction Intermediates)
HDR through Homologous Recombination (HRR)
Homologous DNA Pairing and Strand Exchange
Diseases associated with the TLR signaling cascade
MyD88 deficiency (TLR2/4)
Sensing of DNA DSBs
Immune System
-log(FDR)
log2(Enrichment Ratio)
H
Apoptosis
Viability
Fold-Change
NCS [uM]
0
10
500
*** p_{adj}≤5e-4 ** p_{adj}≤5e-3 * p_{adj}≤0.05 n.s. p_{adj}> 0.05

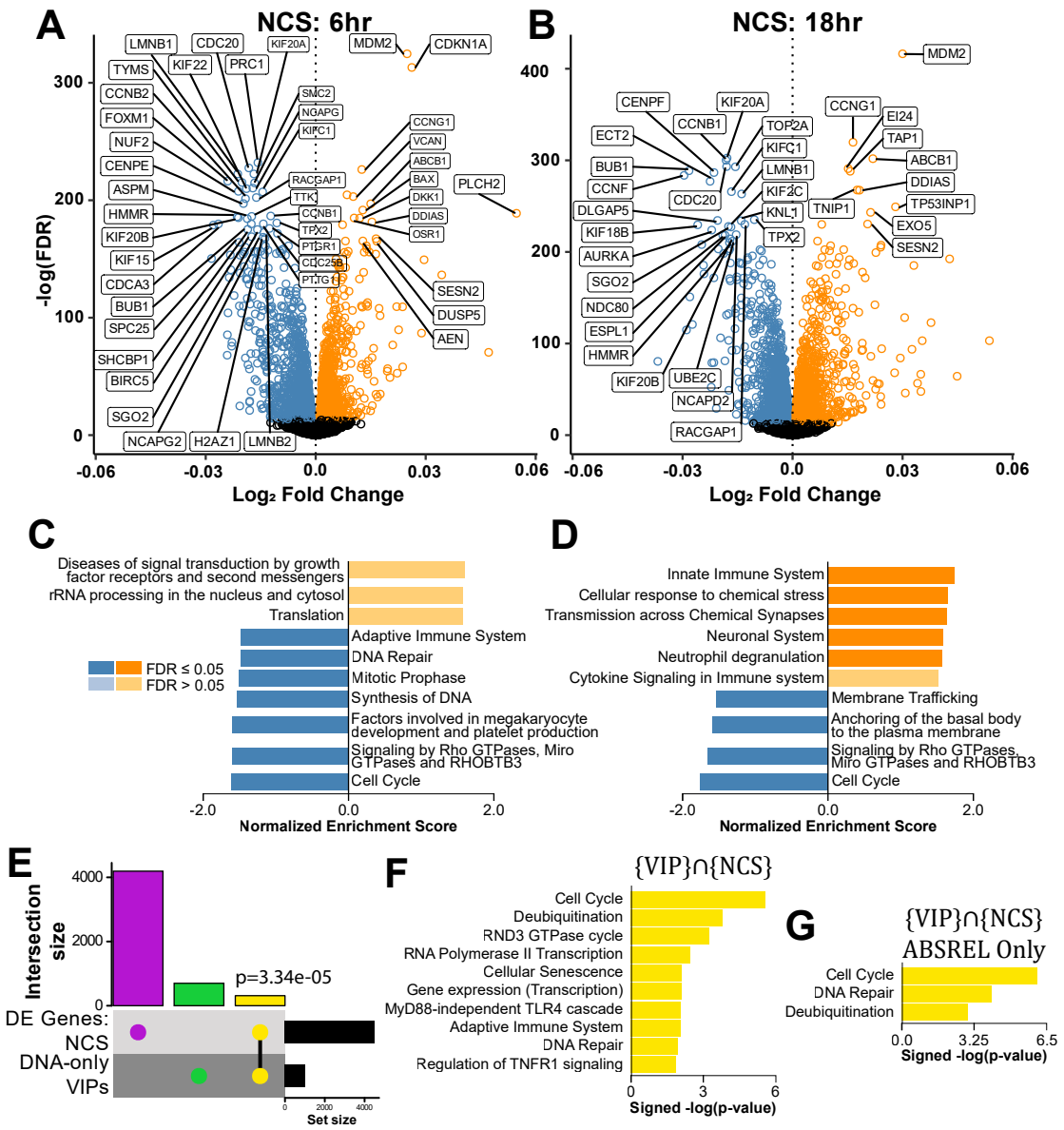
A
NCS: 6hr
-log(FDR)
Log₂ Fold Change
LMNB1
CDC20
KIF20A
MDM2
CDKN1A
TYMS
KIF22
PRC1
CCNB2
FOXM1
NUF2
CENPE
ASPM
HMMR
KIF20B
KIF15
CDCA3
BUB1
SPC25
SHCBP1
BIRC5
SGO2
NCAPG2
H2AZ1
LMNB2
SMC2
NGAPG
KIFC1
CCNG1
VCAN
ABCB1
BAX
DKK1
DDIAS
OSR1
PLCH2
RACGAP1
TTK
CCNB1
TPX2
PTGER1
CDC25B
PTGER4
SESN2
DUSP5
AEN
B
NCS: 18hr
Log₂ Fold Change
MDM2
CENPF
KIF20A
CCNB1
ECT2
BUB1
CCNF
CDC20
DLGAP5
KIF18B
AURKA
SGO2
NDC80
ESPL1
HMMR
KIF20B
UBE2C
NCAPD2
RACGAP1
TOP2A
KIFC1
LMNB1
KIF2C
KNL1
TPX2
CCNG1
EI24
TAP1
ABCB1
DDIAS
TNIP1
TP53INP1
EXO5
SESN2
C
Diseases of signal transduction by growth factor receptors and second messengers
rRNA processing in the nucleus and cytosol
Translation
Adaptive Immune System
DNA Repair
Mitotic Prophase
Synthesis of DNA
Factors involved in megakaryocyte development and platelet production
Signaling by Rho GTPases, Miro GTPases and RHOBTB3
Cell Cycle
FDR ≤ 0.05
FDR > 0.05
Normalized Enrichment Score
D
Innate Immune System
Cellular response to chemical stress
Transmission across Chemical Synapses
Neuronal System
Neutrophil degranulation
Cytokine Signaling in Immune system
Membrane Trafficking
Anchoring of the basal body to the plasma membrane
Signaling by Rho GTPases, Miro GTPases and RHOBTB3
Cell Cycle
Normalized Enrichment Score
E
Intersection size
p=3.34e-05
DE Genes:
NCS
DNA-only
VIPs
Set size
F
{VIP}∩{NCS}
Cell Cycle
Deubiquitination
RND3 GTPase cycle
RNA Polymerase II Transcription
Cellular Senescence
Gene expression (Transcription)
MyD88-independent TLR4 cascade
Adaptive Immune System
DNA Repair
Regulation of TNFR1 signaling
Signed -log(p-value)
G
{VIP}∩{NCS}
ABSREL Only
Cell Cycle
DNA Repair
Deubiquitination
Signed -log(p-value)